Diffraction studies on ordering of quasi-one-dimensional structures and nanowires on silicon surfaces induced by metals

Dissertation (kumulativ)

zur Erlangung des Grades eines
Doktors der Naturwissenschaften (Dr. rer. nat.)

dem Fachbereich Physik der Universität Osnabrück
vorgelegt von

Frederic Yaw Timmer, M. Sc.

Osnabrück, September 2017

Contents

1 Introduction

One-dimensional structures are proposed to exhibit interesting physical properties which differ vastly from the properties observed by structures of higher dimensionality. One such example is the Peierls distortion [1] which minimizes the electronic energy of the one-dimensional system by means of a lattice doubling. Additionally, for one-dimensional systems collective excitations of charges and spins lead to critical behavior described by Tomonaga-Luttinger liquids [2].
In reality, however, it is impossible to fabricate truly one-dimensional materials because they are inherently energetically unstable. Consequently, they must be stabilized by some weak residual interaction with the environment first in order to be observable. One methodology to fabricate such stabilized one-dimensional structures is to grow them on top of the surface of a substrate (which exhibits a higher degree of dimensionality) by self-organization. Due to the interaction with the substrate the one-dimensional structure is stabilized, however, simultaneously this interaction means that the structure is not truly one-dimensional anymore but merely quasi-one-dimensional instead.
Prominent examples of quasi-one-dimensional structures fabricated as described above are the class of metal induced atomic wires (e.g., Si(111)-(5×2)-Au [3, 4, 5, 6] and Au induced atomic wires on Si(hhk) [6, 7, 8]) and the class of rare-earth (e.g., Dy, Tb) silicide nanowires grown on the Si surface [9, 10, 11].
Interpreting experiments regarding e.g., the electronic properties of these type of structures properly requires a firm knowledge of the morphology of these structures as well as the knowledge of their actual atomic structure. Consequently, this thesis is dedicated to the improvement of this (structural) knowledge regarding particularly the aforementioned material systems.
The structural parameters are determined by employing two different diffraction methods in conjunction with kinematic diffraction theory calculations. Spot-Profile Analysis Low-Energy Electron Diffraction experiments are performed in order to determine the morphology of quasi-one-dimensional rare-earth silicide structures on Si(111) and rare-earth silicide nanowires on Si(001) whereas Surface X-Ray Diffraction experiments are performed in order to determine the atomic structure of the metal induced atomic wires of the Si(111)-(5×2)-Au system.
The first part of the thesis (Chapters 2, 3 and 4) contains an overview over the theoretical background, the material systems investigated and the experimental setups used. The second part of the thesis deals with the experiments that were performed and the information derived from them. Here, Chapters 5 and 6 deal with the description and characterization of the quasi-one-dimensional rare-earth silicide structures on Si(111), Chapter 7 deals with the diffraction pattern observed for bundled rare-earth silicide nanowires on Si(001) and the structural information that can be deduced from it and Chapter 8 deals with the determination of the atomic structure of the gold induced atomic wires on Si(111).

2 Theoretical background

In this chapter the theoretical basis of the experimental techniques used is established.

2.1 Crystal structures

2.1.1 Bulk structure

A crystal is a solid in which the atoms, ions or molecules are arranged periodically and infinitely in the three-dimensional space. In such a crystal it is possible to define a sub-unit, the so-called unit cell, and obtain the rest of the crystal by its translation

$$\mathbf{R} = n\mathbf{a} + m\mathbf{b} + p\mathbf{c} \quad \text{with} \quad n, m, p \in \mathbb{Z} \ , \tag{2.1}$$

where the points $\mathbf{R}(n, m, p)$ define the crystal lattice and $\mathbf{a}$, $\mathbf{b}$ and $\mathbf{c}$ are the crystallographic vectors that span the unit cells, see Figure 2.1. The unit cell containing the smallest volume is called the primitive unit cell.
This description is only sufficient for crystals exhibiting only one atom per unit cell, however, in order to describe more complex crystal structures containing multiple atoms per unit cell an (atomic) basis has to be defined. This is done by an additional set of vectors $\mathbf{r}_i$

$$\mathbf{r}_i = u_i\mathbf{a} + v_i\mathbf{b} + w_i\mathbf{c} \ , \tag{2.2}$$

pointing from the origin of the unit cell to the positions of the i atoms (in the unit cell) with their respective coordinates u_i, v_i and w_i (with $0 \leq u_i, v_i, w_i \leq 1$).

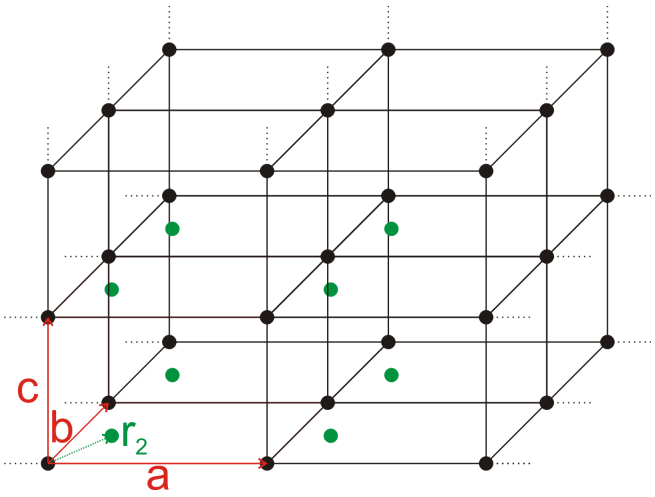

Figure 2.1: Schematical sketch of a crystal with the (primitive) crystallographic lattice vectors **a**, **b**, **c** and a two atomic basis (black, green). In total, eight unit cells are displayed.

In principle, the size of the unit cell can be chosen arbitrarily (in multiples of the primitive unit cell and if the basis is adjusted accordingly), however, in practice most of the time either the primitive unit cell or slightly larger unit cells exhibiting a high degree of symmetry are

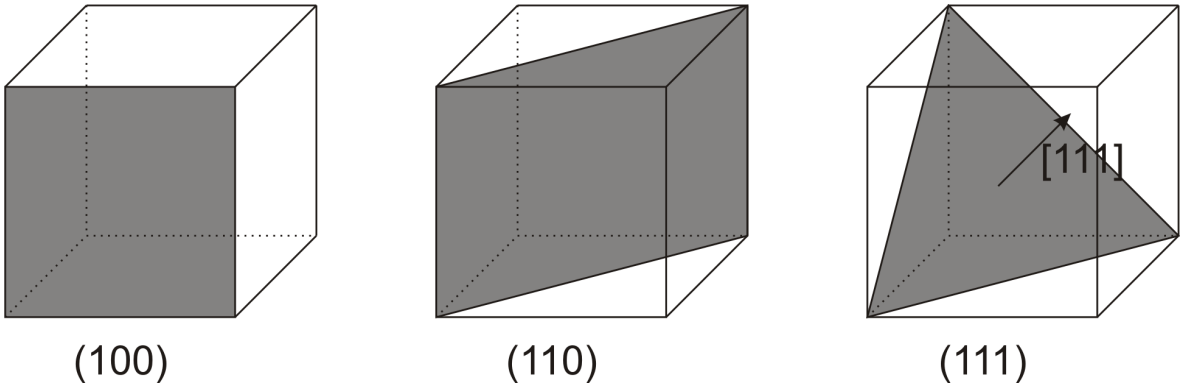

Figure 2.2: Commonly found crystallographic planes in the cubic crystal system (gray).

chosen. In total, there are seven different crystal systems (triclinic, monoclinic, orthorombic, tetragonal, rhombohedral, hexagonal, cubic) which amount to 14 possible Bravais lattices by centering (face-, body-, base-centered).
In order to identify a certain crystallographic plane within a crystal the so-called Miller indices (hkl) are used. In order to obtain the Miller indices of a particular plane first the intercepts of the plane with the crystallographic axes are determined. Thereafter, these values are inverted and reduced to a triplet of integer values with the same ratios (usually the triplet with the smallest integers is taken). The crystallographic direction $[hkl]$ represents a vector normal to this very plane (hkl). Figure 2.2 shows some common crystallographic planes for the cubic lattice system.

2.1.2 Surface structure

In the former section crystals were defined as spatial infinite (periodic) solids. In reality, however, no such thing as an infinite solid can exist, instead every real crystal must exhibit surfaces. These surfaces can also be created artificially by cleavage of the bulk structure in a particular crystallographic plane. At these crystal surfaces the translational symmetry is broken in one (crystallographic) direction which is reflected in the mathematical description of the surface lattice

$$R_s = n_s\mathbf{a}_s + m_s\mathbf{b}_s \quad \text{with} \quad n_s, m_s \in \mathbb{Z} \ , \tag{2.3}$$

where only two crystallographic vectors $\mathbf{a}_s$ and $\mathbf{b}_s$ (parallel to the surface) are needed to describe the periodicity reducing the number of possible types of Bravais lattices from 14 to five (square, rectangular, centered rectangular, hexagonal, oblique). In addition to the change in the mathematical description the physical and chemical properties of the surface may differ from those of the bulk as well (due to e.g. unsaturated atomic bonds, adsorption of atoms). Consequently, the surface as-cleaved might not exhibit the lowest formation energy anymore and may relax into a more energetically favorable structure (e.g. by formation of additional bonds by formerly unsaturated bonds to each other or to adsorbate atoms). This

reconstructed surface (or surface exhibiting a superstructure) usually exhibits a periodicity different from the one observed for the bulk. Again, this surface can be described via the definition of a crystal lattice

$$\mathbf{R}_r = n_r\mathbf{a}_r + m_r\mathbf{b}_r \quad \text{with} \quad n_r, m_r \in \mathbb{Z} \; . \tag{2.4}$$

Here, the crystallographic vectors of the reconstructed surface (or surface exhibiting a superstructure) $\mathbf{a}_r$ and $\mathbf{b}_r$ and the unreconstructed surface $\mathbf{a}_s$ and $\mathbf{b}_s$ can be related to each other. Usually, one of two different methods is used. The more versatile yet less intuitive one is the matrix notation [12] in which the vectors of the reconstructed and unreconstructed surface are related to each other by a matrix

$$\mathbf{a}_r = G_{11}\mathbf{a}_s + G_{12}\mathbf{b}_s \tag{2.5}$$
$$\mathbf{b}_r = G_{21}\mathbf{a}_s + G_{22}\mathbf{b}_s \tag{2.6}$$

with the components G_{ij}. If the reconstructed surface is commensurate to the unreconstructed surface (i.e. $G_{ij} \in \mathbb{Z}$) the more intuitive Wood notation [13]

$$X\,(hkl)\left(\frac{||\mathbf{a}_r||}{||\mathbf{a}||} \times \frac{||\mathbf{b}_r||}{||\mathbf{b}||}\right) - R\varphi^\circ \; , \tag{2.7}$$

can be used. Here, $X(hkl)$ is the surface of the element or compound X with the Miller indices (hkl) and φ° is the rotation between the crystallographic vectors of the reconstructed and the unreconstructed surface.

2.1.3 Reciprocal Lattice

The concept of the reciprocal lattice is very useful for the interpretation of diffraction experiments (e.g. surface X-ray diffraction (SXRD) and low-energy electron diffraction (LEED)). The reciprocal lattice is a set of points represented by the reciprocal lattice vector $\mathbf{G}$ (here given for a three-dimensional crystal)

$$\mathbf{G} = h\mathbf{a^*} + k\mathbf{b^*} + l\mathbf{c^*} \quad \text{with} \quad h, k, l \in \mathbb{Z} \; , \tag{2.8}$$

with the reciprocal crystallographic lattice vectors ($\mathbf{a^*}$, $\mathbf{b^*}$ and $\mathbf{c^*}$) which are related to the crystallographic vectors ($\mathbf{a}$, $\mathbf{b}$ and $\mathbf{c}$) via

$$\mathbf{a^*} = 2\pi\frac{\mathbf{b}\times\mathbf{c}}{\mathbf{a}\cdot(\mathbf{b}\times\mathbf{c})} \; , \quad \mathbf{b^*} = 2\pi\frac{\mathbf{c}\times\mathbf{a}}{\mathbf{a}\cdot(\mathbf{b}\times\mathbf{c})} \; , \quad \mathbf{c^*} = 2\pi\frac{\mathbf{a}\times\mathbf{b}}{\mathbf{a}\cdot(\mathbf{b}\times\mathbf{c})} \; . \tag{2.9}$$

Due to the missing translational symmetry in one crystallographic direction this reduces to

$$\mathbf{G} = h\mathbf{a^*} + k\mathbf{b^*} \quad \text{with} \quad h, k \in \mathbb{Z} \; , \tag{2.10}$$

and

$$\mathbf{a^*} = 2\pi \frac{\mathbf{b} \times \mathbf{n}}{\mathbf{a} \cdot (\mathbf{b} \times \mathbf{n})} \qquad \mathbf{b^*} = 2\pi \frac{\mathbf{n} \times \mathbf{a}}{\mathbf{a} \cdot (\mathbf{b} \times \mathbf{n})} \tag{2.11}$$

for surfaces, where $\mathbf{n}$ is a unit vector normal to the surface. Due to the way the reciprocal crystallographic vectors are constructed they always have the dimension of [1/length] opposed to the crystallographic vectors which have the dimension [length] (hence they are called reciprocal). For surfaces the reciprocal crystallographic vectors and the crystallographic vectors always lie in the same plane and additionally it can be shown that the reciprocal lattice constructed from the crystallographic lattice and the crystallographic lattice itself are always of the same type of Bravais lattice [14].

2.2 Kinematic diffraction theory

The diffraction of electromagnetic waves and electrons is used to characterize the crystal structure of elements, compounds and/or surfaces. In order to gain information about the crystallographic and atomic structure their wavelengths need to be in the order of the atomic distances in the structures investigated (which is in the Å-regime), consequently, x-rays (in the energy range of 5keV-100keV) and electron waves (in the energy range of 10eV-500eV) are used. For the regime in which the interaction between the wave and the material the wave is scattered/diffracted at is small (i.e. only one scattering process between emission and detection of the wave takes place and refraction and absorption are neglected) diffraction phenomena can be described in the kinematic theory of diffraction. In the following chapter the basic concepts of this theory will be explained.

2.2.1 The Laue equation

If electrons or x-rays impinge on a crystal constructive interference can only be observed if the path difference of the waves scattered at different points of the crystallographic lattice exhibits a multiple of the x-ray/electron wavelength for all waves scattered (in the direction of detector). Mathematically this requirement is formulated by the Laue equations

$$\mathbf{qa} = 2\pi h \ , \quad \mathbf{qb} = 2\pi k \ , \quad \mathbf{qc} = 2\pi l \ , \tag{2.12}$$

which can be rearranged to

$$\mathbf{q} = \mathbf{k}_f - \mathbf{k}_i = \mathbf{G} = h\mathbf{a^*} + k\mathbf{b^*} + l\mathbf{c^*} \quad \text{with} \quad h, k, l \in \mathbb{Z} \ , \tag{2.13}$$

by using the definition of the reciprocal lattice (cf. eq. 2.9). Here $\mathbf{k}_i$ is the wave vector of the impinging wave, $\mathbf{k}_f$ is the wave vector of the diffracted wave and $\mathbf{q}$ is the scattering vector (the difference between both) which needs to be a vector to a point in the reciprocal lattice $\mathbf{G}$ at the same time. Consequently, this means for a three-dimensional crystal constructive

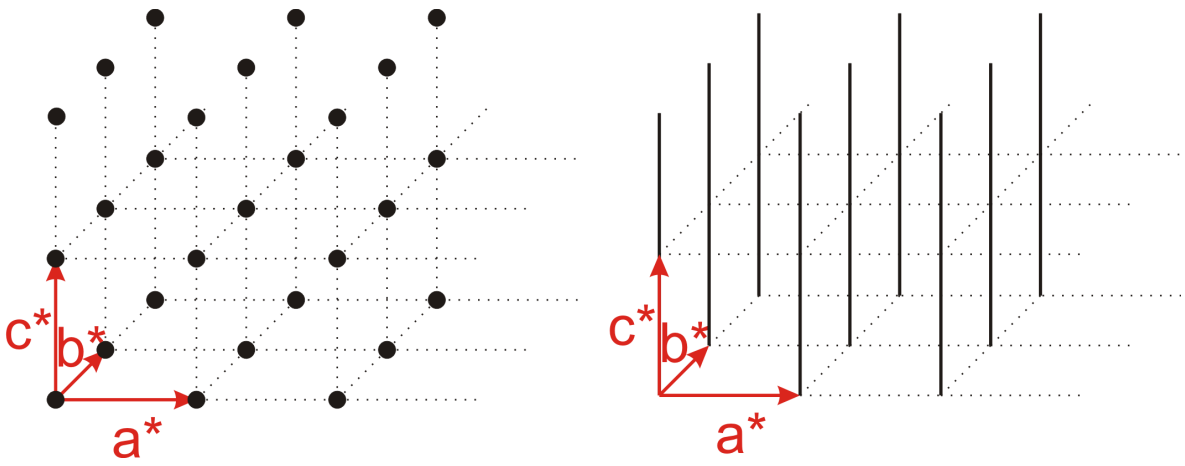

Figure 2.3: Display of the diffraction pattern of a three-dimensional crystal (left) and a (two-dimensional) surface (right). The black dots represent the Bragg peaks whereas the black lines represent the lattice rods, the dotted lines are guides to the eye only.

interference can only be observed at these reciprocal lattice points, the so-called Bragg peaks, see Figure 2.3.

For a surface, however, translational symmetry only exists in two crystallographic directions

$$\mathbf{q}_{\parallel} = (\mathbf{k}_f - \mathbf{k}_i)_{\parallel} = \mathbf{G}_{\parallel} = h\mathbf{a^*} + k\mathbf{b^*} \quad \text{with} \quad h, k \in \mathbb{Z} \ , \tag{2.14}$$

meaning that the momentum perpendicular to the surface $\mathbf{q}_{\perp}$ (here alongside the $\mathbf{c^*}$-direction) can be arbitrarily large without impacting the Laue conditions which only hold true for the part of the momentum projected onto the surface $\mathbf{q}_{\parallel}$. Consequently, instead of Bragg peaks constructive interference is observed on every point along the perpendicular direction meaning that lines of constructive interference, so-called reciprocal lattice rods, can be found in reciprocal space, see Figure 2.3.

Everything explained above only concerns the position of constructive interference (intensity) in reciprocal space which is closely coupled with the periodicity of the unit cell. However, in order to learn more about the atomic structure of the unit cell or the morphology of the surface the absolute intensity and shape of the intensity (lineshape) need to be investigated, respectively. This will be addressed in the following chapters.

2.2.2 Diffraction at a single atom

X-rays are scattered at the electrons of an atom whereas electrons are primarily scattered at the potential exerted by the nucleus of the atom.

Despite these differences the description of the scattering process is analogous for both type of waves. If the position of the atom placed at the origin of the coordinate system (w.l.o.g.) is far away from the position where the scattered wave is detected, the Fraunhofer approximation

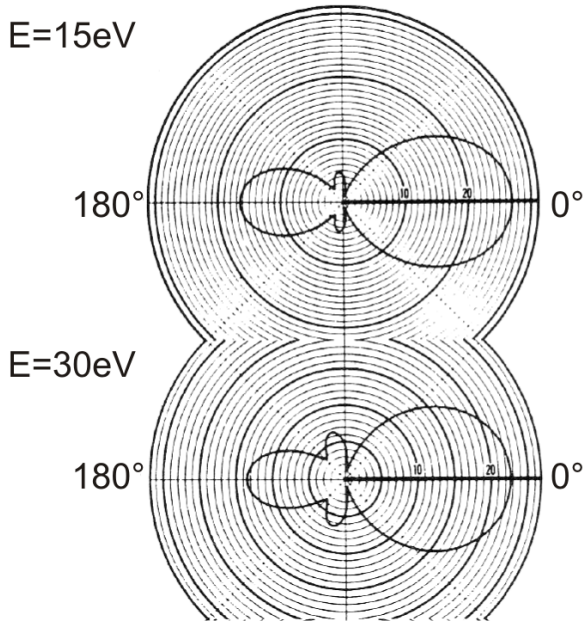

Figure 2.4: Illustration of the square of the scattering amplitude for electrons scattered at energies $E = 15\text{eV}$ and 30eV at platinum showing that low energy electrons are primarily scattered forwards and backwards. Image taken and adapted from [15].

is valid and the amplitude $A_{at}(\mathbf{q})$ of the scattered wave is given by a plane wave

$$A_{at}(\mathbf{q}) \propto f(\mathbf{q}) \exp(i\mathbf{qr}) \,, \tag{2.15}$$

where the atom-dependent part of the amplitude is given by the atomic form factor $f(\mathbf{q})$ and $\mathbf{r}$ is the vector from the point of detection to the position of the atom. Due to the fact that x-rays are scattered isotropically at atoms, the atomic form factor (for x-rays) $f_x(q)$ is only a function of the norm of the scattering vector $\mathbf{q}$ and is given by the sum of the scattering amplitudes at the individual electrons which is equivalent to the Fourier transform of the electron density of the atom which in turn can be approximated by four Gaussian functions

$$f_x(G) = \int d^3r \rho(\mathbf{r}) \exp(i\mathbf{qr}) = \sum_{i=1}^{4} a_i \exp\left(-b_i \left(\frac{q}{4\pi}\right)^2\right) + c \,, \tag{2.16}$$

which are tabulated in [16] for most elements and ions. Atomic form factors for an isotropic electron scattering $f^B(q)$ can be derived from the x-ray atomic form factors $f_x(q)$ by applying the Mott-Bethe formula [16]:

$$f^B(q) = 2\pi \frac{me^2}{h^2 \epsilon_0} [Z - f_x(q)]/q^2 \,, \tag{2.17}$$

however, (for electron energies in the LEED-regime) electrons are not scattered isotropically but show preferential directions instead (forward- and to a lesser extent backward-scattering), see Figure 2.4. Consequently, in order to obtain more accurate atomic form factors $f^B(\mathbf{q})$ dynamical diffraction theory needs to be applied.

2.2.3 Diffraction at a unit cell

The amplitude of the diffraction at a unit cell $A_{uc}(\mathbf{q})$ is given by the summation of the individual scattering amplitudes of the atoms inside the unit cell $A_{at,i}(\mathbf{q})$

$$A_{uc}(\mathbf{q}) \propto \sum_j f_j(\mathbf{q}) \exp\left[i\mathbf{q}(\mathbf{R}+\mathbf{r}_j)\right] = F(\mathbf{q}) \exp\left(i\mathbf{q}\mathbf{R}\right) , \tag{2.18}$$

where $\mathbf{R}$ is the position of the unit cell and $\mathbf{r}_j$ is the position of the j-th atom contained in it (cf. chapter 2.1.1). Additionally, the structure factor of the unit cell $F(\mathbf{q})$ can be defined. It is given by the sum of the atomic form factors $f_j(\mathbf{q})$

$$F(\mathbf{q}) = \sum_j f_j(\mathbf{q}) \exp\left(i\mathbf{q}\mathbf{r}_j\right) , \tag{2.19}$$

thus as the Fourier transform of the electron density in the unit cell. Notably, the structure factor of the unit cell $F(\mathbf{q})$ generally depends on the direction of the scattering vector $\mathbf{q}$ (for structures with more than one atom in the unit cell) even for x-ray diffraction due to the interplay of the different atoms.

2.2.4 Debye-Waller factor

The definition of the structure factor given above (cf. chapter 2.2.3) inherently assumes that the atoms in the unit cells are fixed at particular positions. However, in reality the atoms in a crystal are subject to thermal excitations (at least for temperatures $T \geq 0$ K) manifesting in a dynamic (i.e., time-dependent) vibration of the atoms about their mean position. Additionally, the atomic position of equivalent atoms in the unit cell (in different unit cells) might differ (e.g., due to defects) meaning that there is also a static (i.e., time-independent) component to the deviation from the mean position. Consequently, the structure factor needs to be modified and is given by

$$F(\mathbf{q}) = \sum_j f_j(\mathbf{q}) \exp\left(i\mathbf{q}\mathbf{r}_j\right) \exp\left(-M_j\right) , \tag{2.20}$$

where $\exp(-M_j)$ is the so-called Debye-Waller factor of the j-th atom. Here, M_j, the factor in the exponential function, is given by

$$M_j = 1/2\mathbf{q}^T\mathbf{U}_j\mathbf{q} , \tag{2.21}$$

where $\mathbf{U}_j$ is a symmetric second-order tensor ($u_{ik} = u_{ki}$) representing the "vibrational ellipsoid"

$$U_j = \sum_{i=1}^{3}\sum_{k=1}^{3} u_{jik} \tag{2.22}$$

and the components of the tensor u_{jik} represent the atomic displacement parameters.

2.2.5 Diffraction at a (infinite) single crystal

The amplitude of the diffraction at a single crystal $A_{sc}(\mathbf{q})$ is given by the summation of the amplitude of the individual unit cells $A_{uc,j}(\mathbf{q})$

$$A_{sc} \propto \sum_j F_j(\mathbf{q}) \exp(i\mathbf{q}\mathbf{R}_j) = \sum_j F_j(\mathbf{q}) \exp\left[i\mathbf{q}(n_j\mathbf{a} + m_j\mathbf{b} + p_j\mathbf{c})\right] , \tag{2.23}$$

where $\mathbf{R}_j = n_j\mathbf{a} + m_j\mathbf{b} + p_j\mathbf{c}$ denotes the position and $F_j(\mathbf{q})$ the structure factor of the j-th unit cell. Assuming a crystal with a spatial extension of a number of N_a, N_b and N_c similar unit cells (in the respective crystallographic directions) this can be rearranged to

$$A_{sc} \propto F(\mathbf{q}) \sum_{n=0}^{N_a-1} \exp(2\pi ihn) \sum_{m=0}^{N_b-1} \exp(2\pi ikm) \sum_{p=0}^{N_c-1} \exp(2\pi ilp) \propto B(h, N_a)\, B(k, N_b)\, B(l, N_c) . \tag{2.24}$$

which essentially is a product of three similar sums B. These sums can be identified as geometric series (here only displayed for one particular direction)

$$B(h, N_a) = \sum_{n=0}^{N_a-1} \exp(2\pi ihn) = \frac{1 - \exp(2\pi ihN_a)}{1 - \exp(2\pi ih)} . \tag{2.25}$$

Its absolute square is given by

$$S(h, N_a) = |B(h, N_a)|^2 = \frac{\sin^2(\pi hN_a)}{\sin^2(\pi h)}, \tag{2.26}$$

which is equivalent to the N-slit function $S(h, N_a)$ displaying $N_a - 1$ maxima (in the interval of $\Delta h = 1$), cf. Figure 2.5. Here, maxima located at integer values $h \in \mathbb{Z}$ always exhibit more intensity than the maxima observed at fractional values. Increasing the number of atoms N_a in the particular crystallographic direction increases the number of maxima observed. Consequently, the full width at half maximum (FWHM) of these maxima decreases.

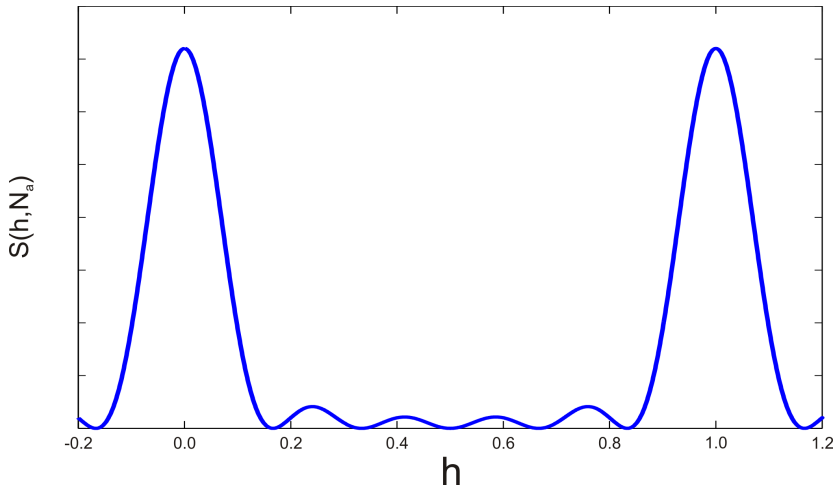

Figure 2.5: N-slit function for $N_a = 6$ exhibiting five maxima in the interval $\Delta h = 1$.

Additionally, intensity is redistributed from the fractional to the integer maxima. For the limes of an infinite number of atoms N_a

$$\lim_{N_a \to \infty} S\left(h, N_a\right) = \delta(\nu - h) \quad \text{with} \quad \nu \in \mathbb{Z} \; , \tag{2.27}$$

all intensity is confined to the integer maxima which exhibit a negligible FWHM and can thus be interpreted as a representation of the delta-distribution δ. Applying the same formalism for the other two directions the intensity of the (infinite) crystal is given by

$$\left|A_{sc}\right|^2 \propto \left|F\left(\mathbf{q}\right)\right|^2 \delta(\nu - h)\delta(\mu - k)\delta(\tau - l) = \left|F\left(\mathbf{q}\right)\right|^2 G_{lat}\left(\mathbf{q}\right) \quad \nu, \mu, \tau \in \mathrm{Z} \; . \tag{2.28}$$

Here, the lattice factor $G_{lat}\left(\mathbf{q}\right)$ is essentially a reformulation of the Laue equation for a three dimensional (infinite) crystal (cf. chapter 2.2.1) determining the points in reciprocal space where intensity can be observed whereas the absolute square of the structure factor $\left|F\left(\mathbf{q}\right)\right|^2$ determines their intensity.

2.2.6 Diffraction at a crystal surface

The concept of an infinite crystal is not very realistic, however. In order to be able to compare theoretical calculations with experimental diffraction data obtained from crystal surfaces a more realistic model needs to be employed.
In reality, every crystal exhibits surfaces. If such a crystal surface is radiated by an x-ray beam the beam penetrates the surface and passes through the crystal for a particular distance before it is diffracted. Due to the fact that the interaction between matter and x-rays is relatively weak x-rays exhibit a large penetration depth ($\sim \mu$m) and penetrate a large number of crystal layers which all contribute to the diffracted intensity. Nevertheless, the intensity of the x-ray

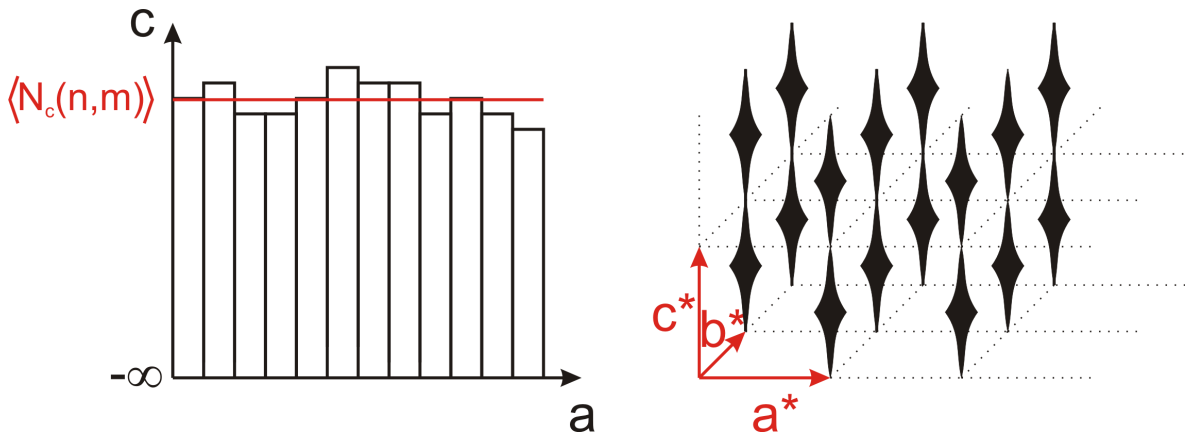

Figure 2.6: (a) Schematic display of a rough (semi-infinite) crystal surface projected onto the *ac*-plane. The average of the height function $N_c(n,m)$ is displayed as well. (b) Display of the diffraction pattern of the rough surface in (a) exhibiting crystal truncation rods which show maximum intensity at the nominal Bragg peak positions.

beam is decreased by absorption (and reflection) during the pass through, by the factor ϵ per layer, meaning that x-rays diffracted at deeper layers are weaker on average and contribute less strongly to the diffracted intensity.

If the crystal is significantly thicker than the x-ray penetration depth it can be assumed to be semi-infinite in the direction perpendicular to the surface. Additionally, the surface does not have to be homogeneous necessarily (i.e., exhibit the same height everywhere), but can exhibit roughness (described by the height function $N_c(n,m)$) instead, see Figure 2.6. The diffracted amplitude of such a rough crystal surface A_{cs} is given by

$$A_{cs} \propto F(\mathbf{q}) \sum_{n=0}^{N_a-1} \exp(2\pi i h n) \sum_{m=0}^{N_b-1} \exp(2\pi i k m) \sum_{p=-\infty}^{N_c(n,m)-1} \exp(p(2\pi i l + \epsilon)) \,, \tag{2.29}$$

which can be rearranged to

$$A_{cs} \propto F(\mathbf{q}) \sum_{n=0}^{\infty} \sum_{m=0}^{\infty} \frac{\exp(N_c(n,m)(2\pi i l + \epsilon))}{1 - \exp(-(2\pi i l + \epsilon))} \,, \tag{2.30}$$

if a macroscopic sample (i.e., $n, m \to \infty$) is considered. This essentially equates to the spatial averaging of the height function $N_c(n,m)$

$$A_{cs} \propto F(\mathbf{q}) \frac{\langle \exp(N_c(n,m)(2\pi i l + \epsilon)) \rangle}{1 - \exp(-(2\pi i l + \epsilon))} \tag{2.31}$$

which can be rearranged to

$$A_{cs} \propto F(\mathbf{q}) \frac{\exp\left(-\sigma^2 (1-\cos 2\pi l)\right)}{1-\exp\left(-(2\pi i l+\epsilon)\right)} \ , \tag{2.32}$$

where σ is the root mean square of the surface roughness, if the height function $N_c(n,m)$ is assumed to be Gaussian shaped [17].
Analyzing equation 2.32 shows that no sharp Bragg peaks (with respect to l) can be observed in the diffraction pattern. Instead, so-called crystal truncation rods (CTR) exhibiting intensity everywhere perpendicular to the surface are observed in reciprocal space (for $h,k \in \mathbb{Z}$), see Figure 2.6. These CTRs exhibit maximum intensity at the nominal Bragg peak positions and minimum intensity between two nominal Bragg peak positions.

2.2.7 Diffraction at a reconstructed surface

The reconstruction or superstructure of a surface (induced by e.g. bonding of unsaturated bonds to each other or to adsorbate atoms) usually reaches only several atomic layers deep into the crystal. Additionally, there is no repetition of the reconstructed unit cell perpendicular to the surface. Consequently, there is neither a Laue condition nor a formation of CTRs perpendicular to the surface and the intensity is given by

$$|A_{rs}|^2 \propto |F(\mathbf{q})|^2 \delta(n-h)\delta(m-k) = |F(\mathbf{q})|^2 G_{lat}(\mathbf{q}) \quad n,m \in \mathrm{Z} \ , \tag{2.33}$$

meaning that intensity can be observed on lattice rods (along the **c***-direction for $h,k \in \mathbb{Z}$, as predicted in chapter 2.2.1) in the reciprocal space and the intensity along the lattice rods is given by the absolute square of the structure factor $|F(\mathbf{q})|^2$.

2.2.8 Diffraction at a disordered surface

Until now we assumed the surface to be void of e.g., point defects, domain boundaries (DBs) or dislocations. For disordered surfaces, see Figure 2.7, the long-range periodicity is not necessarily given and the Laue conditions are either blurred or non-existent dependent on the degree of disorder. Consequently, the amplitude of the diffracted wave A_{ds} is given by

$$A_{ds}(\mathbf{q}) \propto \sum_j F_j(\mathbf{q}) \exp(i\mathbf{q}\mathbf{R}_j) = N \langle F_j(\mathbf{q}) \exp(i\mathbf{q}\mathbf{R}_j)\rangle_j = N \langle F(\mathbf{q}) \exp(i\mathbf{q}\mathbf{R})\rangle \ , \tag{2.34}$$

which is the spatial average of the arrangement of the unit cells on the disordered surface (morphology).
Consequently, the intensity is given by

$$|A_{ds}(\mathbf{q})|^2 \propto \sum_n \langle F_j(\mathbf{q}) F_n^*(\mathbf{q}) \exp(i\mathbf{q}[\mathbf{R}_j - \mathbf{R}_n])\rangle_j = |F(\mathbf{q})|^2 G_{lat}(\mathbf{q}) \ , \tag{2.35}$$

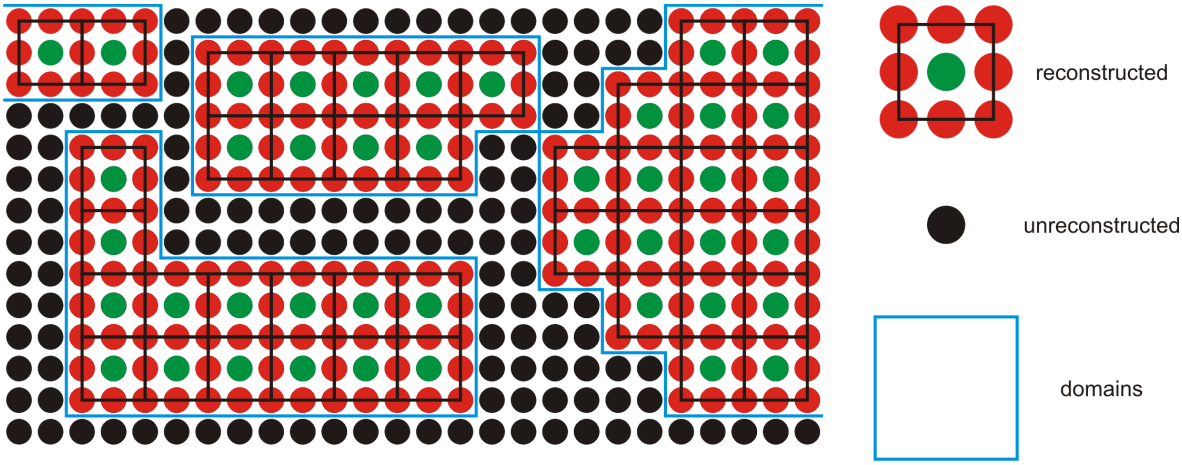

Figure 2.7: Schematic sketch of a disordered surface (top view) exhibiting different domains of the same reconstruction (encased in blue) separated by unreconstructed parts of the surface.

and depends on the structure factor $|F(\mathbf{q})|^2$ and on the arrangement of the unit cells in real space (in contrast to ordered surfaces). However, it can be shown that the arrangement of unit cells in real space does not impact the (absolute) magnitude of the intensity in the Brillouin zone [18] but instead induces a redistribution of the intensity changing the lineshape of peaks and lattice rods. Consequently, the morphology or at least central quantities determining the morphology can be deduced from the investigation of the lineshape.

2.2.9 Electron diffraction

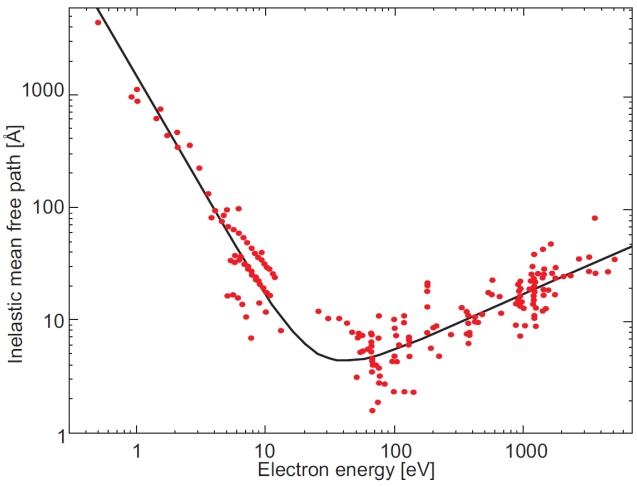

Figure 2.8: Inelastic mean free path as a function of electron energy. Image taken from [19].

Electrons with the energy E can be described as electron waves (de Broglie waves) with the

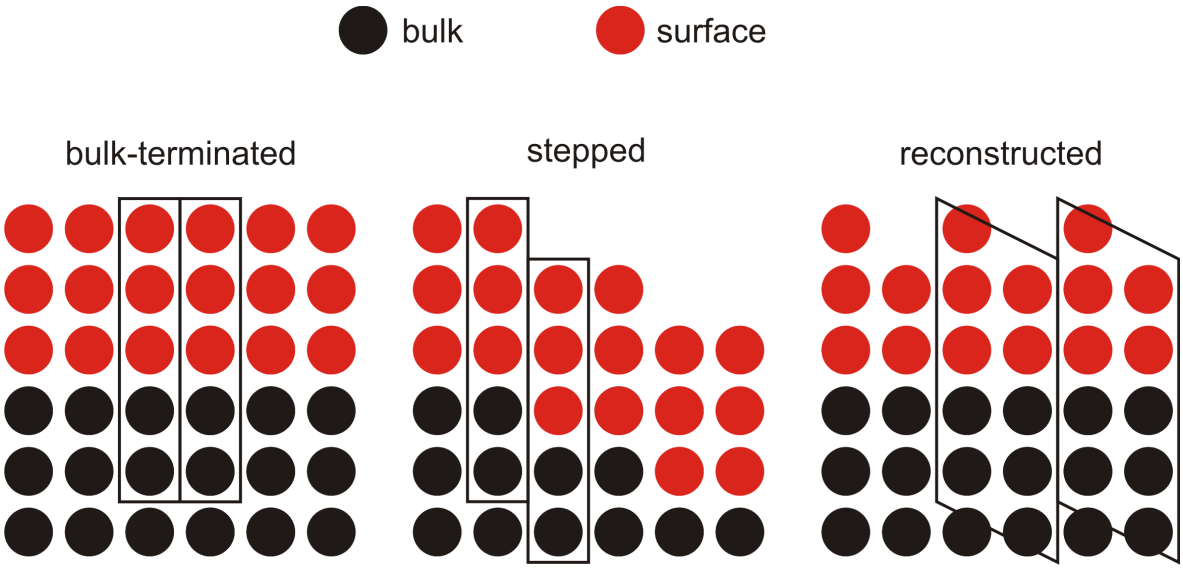

Figure 2.9: Schematic sketch of column-like unit cells (black boxes) used in the description of electron diffraction for three different type of surfaces (bulk-terminated, stepped and a reconstructed surface).

wavelength

$$\lambda = \frac{h}{\sqrt{2m_e E}} \ , \tag{2.36}$$

where h is the Planck constant and m_e is the rest mass of the electron. Figure 2.8 shows the inelastic mean free path (IMFP) of these electron waves in matter as a function of electron energy showcasing that the interaction between matter and electrons is strong ($IMFP \approx 10$ Å) for the LEED energy regime (10eV-1000eV). Consequently, the average number of scattering processes of an electron (in a crystal) is significantly higher than one (which violates the assumptions made for the kinematic diffraction theory). In order to understand the implications of the multiple scattering on the intensity of the diffracted electrons dynamical diffraction theory needs to be applied eventually enabling the determination of the atomic structure of the unit cell (among other properties). However, in order to investigate the crystallography and morphology multiple scattering can be disregarded and employing an approach based on the kinematic theory of diffraction is sufficient [18]. Due to the low penetration depth of the electrons column-like unit cells extending several atomic layers into the surface are sufficient to describe diffraction completely, see Figure 2.9. Consequently, the diffraction pattern is surface-like independent of the sample investigated.

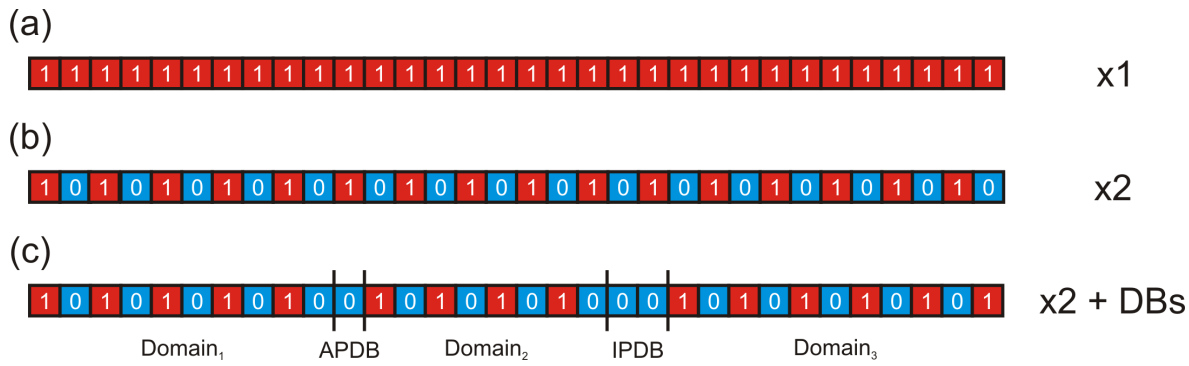

Figure 2.10: Display of three different binary surfaces with an array length $m = 32$ (a) a perfect one-fold periodicity, (b) a perfect two-fold periodicity and (c) a two-fold periodicity with in-phase and anti-phase DBs.

2.3 Binary surface technique

The following sections explain the binary surface technique [20] which is used to simulate the diffraction pattern of (disordered) surfaces and determine the domain and domain boundary distributions by comparison to experimental diffraction data.

2.3.1 Binary surface

The crystallographic lattice is parametrized by a binary array with the sizes $m \times p$ with periodic boundary conditions. Ones ([1] in the binary array) correspond to scattering centers (i.e. atoms or unit cells) whereas no scattering takes place at zeros ([0] in the binary array). In this work, specifically, the surfaces under investigation exhibit a strong (quasi-)one-dimensional character. Consequently, it is sufficient to describe the surface by an one dimensional binary array (with the size $m \times p = m \times 1$). Different periodicities can be realized by different binary sequences. The unit cell of e.g. a one-fold periodicity is represented by a simple $D = [1]$ whereas a two-fold periodicity can be represented either as $D_1 = [1\ 0]$ or $D_2 = [0\ 1]$.
Constructing a surface of a particular periodicity is achieved by appending unit cells of the desired periodicity until the maximum array size m is reached. For instance, the sequences displayed in Figure 2.10(a)-(b) show a perfect one- and two-fold periodicity for the array length $m = 32$.

DBs can be introduced by inserting structural motifs breaking the predominant periodicity, see Figure 2.10(c), e.g. through the introduction of an additional [1] or [0] between (similar) adjacent unit cells of a two-fold periodicity. Two different types of DBs can be discriminated in this description. Depending on the character of the DB adjacent domains are shifted by a fraction or a multiple of the size of the unit cell. Anti-phase domain boundaries (APDBs) have a width fractional to the periodicity they are embedded in (e.g. $DB_1 = [0]$ for a two-fold periodicity) and consequently shift the phase by a fraction. In-phase domain boundaries (IPDBs), however, exhibit a width that is a multiple of the periodicity they are embedded in (e.g. $DB_2 = [0\ 0]$ for a two-fold periodicity) meaning there is no phase shift between adjacent

domains.
Introducing N DBs the surface is composed of N domains (e.g. reconstructed with a two-fold periodicity) separated by these domain boundaries. Consequently, a mean domain size $\langle\gamma\rangle$ and its variance σ^2 can be defined,

$$\langle\gamma\rangle = \frac{1}{N}\sum_{i=1}^{N}\gamma_i \quad \text{and} \quad \sigma^2 = \frac{1}{N}\sum_{i=1}^{N}\left(\gamma_i - \langle\gamma\rangle\right)^2 , \tag{2.37}$$

which equate to the first and second momentum of the individual domain sizes γ_i.
Reversely, this means that a surface with a certain mean domain size $\langle\gamma\rangle$ can be created by appending domains with a domain size γ chosen by random numbers following a domain size distribution $P(\gamma)$

$$P(\gamma) = P\left(\gamma, \langle\gamma\rangle, \sigma^2\right) \quad \text{with} \quad \sum P\left(\gamma, \langle\gamma\rangle, \sigma^2\right)\gamma = \langle\gamma\rangle \ . \tag{2.38}$$

But not only the domain size can be distributed but the size of the DBs as well. Additionally, different types of DBs/Domains can be alternated, statistically mixed or distributed (by any kind of distribution) so that basically any configuration of the surface can be realized.

2.3.2 Obtaining the simulated diffraction pattern

In order to obtain the simulated diffraction pattern of a surface with a particular domain size- and domain boundary distribution, n different surfaces following these distributions are created. Due to the fact that the individual surfaces are created by random numbers (following the respective distributions) each surface is a different representation of the underlying distributions. Subsequently, the absolute square of the Fourier transform of the individual surfaces is computed, which equates to the intensity $I(\mathbf{q})$ of the individual surface. Eventually, the intensity $I(\mathbf{q})$ of all surfaces are superimposed incoherently to obtain the simulated diffraction pattern of the sample. This methodology is equivalent to the situation in a real diffraction experiment where different regions on the sample (which are representations of the underlying distributions of the sample) are probed individually, due to a limited coherence length of the electron waves. Here, the intensity is given by the incoherent superposition of the intensity of the individual regions as well.

2.3.3 Determination of domain and domain boundary distributions

In order to be able to determine domain and/or domain boundary distributions first the simulated and the experimental diffraction patterns need to be made comparable.
Every experimentally recorded diffraction pattern I_{exp} is broadened by experimental uncertainty, which is intrinsic to the apparatus the diffraction pattern was recorded with. The experimental error can be described by the instrument function $T(\mathbf{q})$, which can be derived from the diffraction pattern of a nearly ideally ordered surface (e.g. 7×7-Si(111)). The

recorded diffraction pattern I_{exp} is given by the convolution of the ideal diffraction pattern I_{ideal} and the instrument function T [21]

$$I_{exp} = I_{ideal} \otimes T \ . \tag{2.39}$$

Consequently, the simulated diffraction pattern I_{th} needs to be convoluted with the instrument function T

$$I_{cth} = I_{th} \otimes T \ , \tag{2.40}$$

in order to obtain the convoluted simulated diffraction pattern I_{cth}, which can be compared to the experimentally recorded diffraction pattern I_{exp}.
The deviation of the convoluted simulated diffraction pattern I_{cth} and the experimentally recorded diffraction pattern I_{exp} is quantified by either the mean squared error (MSE)

$$MSE = \frac{1}{n} \sum_{i=1}^{n} \left(I_{cth,i} - I_{exp,i} \right)^2 \ , \tag{2.41}$$

or the Pendry R-factor [22]

$$R = \int \left(Y_{cth} - Y_{exp} \right)^2 \mathrm{d}q_{\parallel} / \int \left(Y_{cth}^2 + Y_{exp}^2 \right) \mathrm{d}q_{\parallel} \ , \tag{2.42}$$

with

$$Y = L^{-1} / \left(L^{-2} + c^2 \right) \quad \text{and} \quad L = I / I' \ , \tag{2.43}$$

where c is a factor which is proportional to the width of the peaks observed in the (experimental) diffraction pattern. If only a small fraction of the reciprocal space is considered, comparison by means of the MSE is sufficient, however, due to dynamical effects (influencing mainly the absolute intensity in the diffraction pattern and not the lineshape itself) for larger fractions of the reciprocal space the Pendry R-factor is used which is less sensitive to these differences in absolute intensity but rather is sensitive to peak positions and shapes.
Now, in order to determine the domain and/or domain boundary distributions of a particular (disordered) surface, the underlying distributions of the surface (cf. equation 2.38) are varied until the deviation of the theoretical I_{cth} and the experimental diffraction pattern I_{exp} is minimized.

2.4 Determination of the atomic structure by SXRD

Due to the fact that the interaction between x-rays and matter is relatively weak, for SXRD experiments, the samples are irradiated with x-rays under a grazing angle of incidence (slightly

higher than the angle of total reflection) in order to increase the surface sensitivity. Subsequently, intensity is recorded at certain spots in reciprocal space allowing for a direct determination of basic structural elements of the surface. Afterwards, from these basic structural elements a so-called starting model can be derived which in turn can be improved by comparison of the experimentally recorded and the calculated intensity from this very model. In the following chapter the basics of this method and the physics behind it are explained.

2.4.1 Reflection and refraction of x-rays at interfaces

The reflection and refraction of x-ray radiation can be described by the complex refractive index n

$$n = 1 - \delta + i\beta \ , \tag{2.44}$$

where β is the absorption and δ the dispersion, which are proportional to the electron density of the material and the wavelength of the the x-rays. At an interface between two different materials the refractive index n changes. Due to this abrupt change in the electron density one part of the x-ray beam is refracted (transmitting into the new material) while the other part is reflected. The angle α_2 under which the beam propagates in the new medium n_2 is different from the incident angle α_1. The change in direction is given by Snell's law

$$n_1 \cos\alpha_1 = n_2 \cos\alpha_2 \ . \tag{2.45}$$

Due to the fact that the refractive index of matter $n_2 = n_{mat}$ is always smaller than unity it is also smaller than the refractive index of air ($n_1 = n_{air} \sim 1$) or vacuum ($n_1 = n_{vac} = 1$). Consequently, the angle under which the x-ray beam propagates in the new medium (coming from vacuum going into matter) is always smaller than the angle of incidence of the x-ray beam ($\alpha_2 \leq \alpha_1$). Accordingly, there is a lower limit for the angle of incidence (the critical angle α_c) where x-ray beams cannot penetrate into the matter anymore and instead are reflected totally. The critical angle can be approximated by

$$\alpha_c = \sqrt{2\delta_{mat}} \ , \tag{2.46}$$

which equates to $\alpha_c \sim 0.10°$ - $0.25°$ (for dispersions in the order of $\delta \sim 10^{-6}$ which is realistic for photon energies of $E \sim$ 10keV-20keV).

2.4.2 Patterson function

The structure factor $\mathrm{F}(\mathbf{q})$ is equivalent to the Fourier transform of the charge density of the atoms in the unit cell. However, experimentally it is only possible to derive the absolute square of the structure factor $\mathrm{F}|(\mathbf{q})|^2$ and not the structure factor $\mathrm{F}(\mathbf{q})$ itself. Consequently, the phase information is missing and the atomic structure inside the unit cell cannot be derived directly

from the intensity collected in an x-ray diffraction experiment. This is commonly referred to as the phase problem. One approach to derive structural information despite the phase problem is to apply the so-called Patterson function $P\left(U,V,W\right)$

$$P(U,V,W) = \sum_{j}^{N} \left|F\left(h_j,k_j,l_j\right)\right|^2 e^{-2\pi i(h_jU+k_jV+l_jW)} \ , \tag{2.47}$$

where $|F|^2$ is the absolute square of the structure factor of the intensity observed at the point

$$\mathbf{G}_j = h_j\mathbf{a^*} + k_j\mathbf{b^*} + l_j\mathbf{c^*} \tag{2.48}$$

in reciprocal space. The Patterson function is equivalent to the Fourier transform of the absolute square of the structure factor $\mathrm{F}|(\mathbf{q})|^2$, which in turn is equivalent to the auto-correlation (= self-convolution) of the charge density. Consequently, the maxima in the Patterson function can be interpreted as inter-atomic distances in the unit cell rather than as positions of atoms in the unit cell. Additionally, the intensity of the maxima observed in the Patterson function $P\left(U,V,W\right)$ is proportional to the product of the atomic numbers of the atoms causing it ($Z_i \times Z_j$). Therefore, especially distances between the heavier atoms in the atomic structure are emphasized.
In practice, (usually) only the projection into the xy-plane of the Patterson function $P\left(U,V\right)$ is generated (by taking into account only structure factors $F\left(\mathbf{q}_j\right)$ at positions with negligible out-of-plane momentum $l_j \sim 0$)

$$P(U,V) = \sum_{j}^{N} \left|F(h_j,k_j,l_j=0)\right|^2 e^{-2\pi i(h_jU+k_jV)} \ , \tag{2.49}$$

reducing the dimensionality of the Patterson function from three to two dimensions in order to reduce its complexity. Consequently, the inter-atomic distances are projected into the xy-plane. Analyzing the Patterson function (i.e., finding the inter-atomic distances) it is possible to create an initial atomic structure model or estimate the validity of atomic structure models derived by other experimental and/or theoretical methods.

2.4.3 Structural refinement

In order to refine an atomic structure with reference to experimental data, first a metric quantifying the agreement between the measured structure factor F_{exp} and the computed structure factor for the atomic structure model F_{model} needs to be defined. In principle, there is a vast amount of functions to choose from, however, the most widely spread function in the SXRD-community is the χ^2-function

$$\chi^2 = \frac{1}{N}\sum_{i=1}^{N} \frac{\left(|F_{i,exp}|^2 - |F_{i,model}|^2\right)^2}{\sigma_{i,exp}^2} \ . \tag{2.50}$$

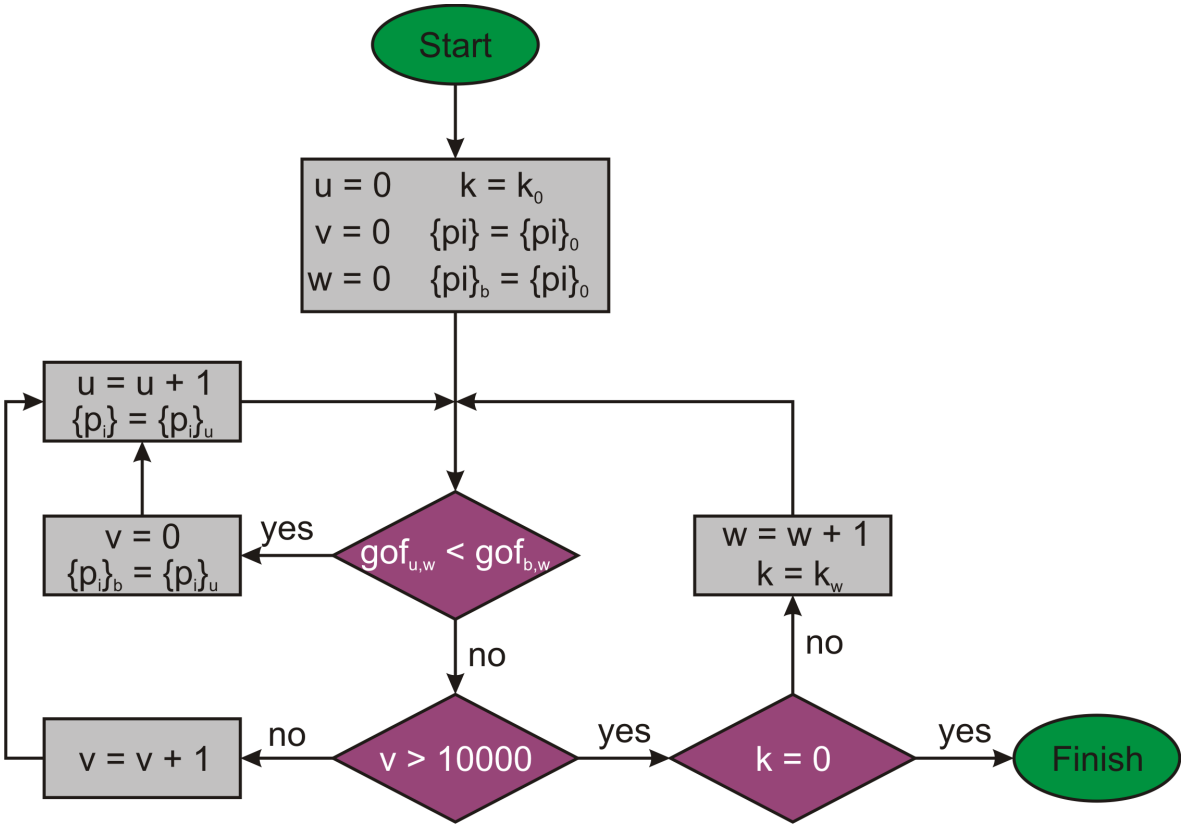

Figure 2.11: Flowchart of the algorithm used to refine the structure(s) in this thesis. For explanation, see text.

Here, the difference in the absolute square of the experimental $F_{i,exp}$ structure factor for a particular reflection ($\equiv$ intensity at a particular point in reciprocal space $\mathbf{G}_i$) and the computed structure factor $F_{i,model}$ for this reflection is weighted by the experimental error $\sigma_{i,exp}$ attached to the reflection. In the first order approximation, the experimental error of a reflection is equal to the statistical error which in turn is proportional to the square root of its intensity [23]. Consequently, the higher the experimental intensity of a given reflection the stronger its influence on the χ^2-function.

In order to refine a (starting) model properties of the model need to be changed (e.g., the x-, y-, z-components of the atomic positions) during refinement. These properties, the so-called free parameters of the refinement p_i need to be defined before the start of the refinement procedure. If a structure model contains N atoms and every atom is allowed to move in every direction independently during the refinement procedure the number of free parameters i is equal to $3N$. However, the movement of the atoms, needs to be defined in such a way that the symmetry imposed on the structure model is conserved. Consequently, it is possible that the movement of certain atoms in the structure model is coupled (e.g., due to mirror planes or n-fold rotation axes) reducing the number of free parameters i. For each iteration u during

the refinement procedure a new set of free parameters $\{p_i\} = \{p_i\}_u$ is generated (derived from the current best set of parameters $\{p_i\}_b$ by an algorithm). Subsequently, the structure model (derived by applying the values of the new set of free parameter $\{p_i\}_u$ to the starting model) is compared to the experimental data.
However, the larger the number of free parameters i the smaller the contribution of the individual parameter p_i to the structure factor F_{model}. Consequently, it is possible that physically unreasonable atomic positions (i.e., for example two (bond) atoms moving very close to each other) for individual atoms still lead to an overall better χ^2-value especially if the refinement is still far away from the global minimum. This either leads to a decrease in the rate of convergence or in some cases even to the trapping of the algorithm in a local minimum instead of finding the global minimum. Therefore, the function quantifying the agreement (goodness of fit $\equiv gof$) is modified to

$$gof_{u,w} = \chi^2(u) + k(w)E_{Keat}(u) \ , \tag{2.51}$$

where $k(w)$ is a proportionality factor weighting the Keating energy E_{Keat} (cf. chapter 2.4.4) of the structure model (with the parameter set $\{p_i\}_u$) in respect to its $\chi^2(u)$-function which is decreased gradually during the refinement process

$$k_{w+1} < k_w \ . \tag{2.52}$$

This means not only the agreement between the structure factors (of the experiment and the model) but also the inner energy of the model is considered during refinement. Consequently, the algorithm does not get stuck in local minima (caused by physically unreasonable bond length/angles) that easily.
If the $gof_{u,w}$ of a (new) model $\{p_i\}_u$ is lower than the $gof_{b,w}$ of the (old) best model $\{p_i\}_b$ its parameters are saved as the (new) best model $\{p_i\}_b = \{p_i\}_u$. This process is repeated until the global minimum (for a particular value $k(w) = k_w$) is found ($\equiv$ no change in the $gof_{b,w}$ for $v = 10000$ consecutive parameter sets). Subsequently, the proportionality factor $k(w)$ is decreased

$$k(w) = k_{w+1} \ , \tag{2.53}$$

and after this the global minimum is searched for again.
This search for the global minimum for a particular value of the proportionality factor $k(w)$ followed by its decrease is alternated until the global minimum for $k_w = k_{end} = 0$ is found, see Figure 2.11 for the flowchart of the refinement procedure. This means that the $gof_{u,w}$ reduces to the χ^2-function for $k(w) \sim 0$ (close to the global minimum of the refinement procedure) eventually also allowing for less energetically favorable atomic configurations which might be observed in reality.

2.4.4 Keating Energy

The elastic energy for elements or compounds (exhibiting covalent bonds) can be approximated by the so-called Keating energy [24, 25]

$$E_{Keat} = \sum_{ij} \frac{\alpha_i + \alpha_j}{2} \left(\mathbf{r}_{ij}^2 - (c_i + c_j)^2\right)^2 + \sum_{ijk} \beta_i \left(\mathbf{r}_{ij}\mathbf{r}_{ik} + w_{ijk}(c_i + c_j)(c_i + c_k)\right)^2 \ . \quad (2.54)$$

Here, the c's are the covalent radii of the particular atoms, the $\mathbf{r}$'s are vectors from one particular atom to another particular atom (which form a (chemical) bond), the α's and β's are element specific constants (for Si and Ge cf. [25]) and w_{ijk} is a factor dependent on the ideal angle between two bonds (which go out from one mutual atom). For structures containing only atoms of one element which are sp^3 hybridized (e.g., Si, Ge) this can be simplified to

$$E_{Keat} = \alpha \sum_{ij} \left(\mathbf{r}_{ij}^2 - r_0^2\right)^2 + \beta \sum_{ijk} \left(\mathbf{r}_{ij}\mathbf{r}_{ik} + w r_0^2\right)^2 \ , \quad (2.55)$$

where r_0 is the (covalent) bond length and $w_{ijk} = \mathrm{w} = 1/3$. In total, there are two contributions to the elastic energy (given by two sums). The first sum reflects the additional energy necessary to compensate for the deviation from the ideal bond length and the second sum reflects the additional energy necessary to compensate for the deviation from the ideal bond angle (and to a lesser extent also to the deviation from the ideal bond length). Consequently, the elastic energy for a perfectly ordered crystal (Si, Ge) is zero.
A Keating energy analysis (i.e., minimization of the Keating energy E_{Keat} by variation of the atomic positions) cannot be used to find new structure models due to the fact that bonds between atoms need to be predefined and neither (new) bonds can be formed nor (existing) bonds can be broken during it. However, a Keating analysis can be used to supplement the refinement of atomic structures by e.g., SXRD (cf. chapter 2.4.3).

2.5 Auger electron spectroscopy

The Auger electron spectroscopy is based on the Auger effect. Here, a primary electron is removed from the atom (by either electrons or photons) leaving behind a vacancy in an orbital at the energy level $-E_{B,1}$ (with respect to the Fermi energy E_F). Subsequently, this vacancy is filled by a second electron from an orbital at a higher energy $-E_{B,2}$. Consequently, there is an energy difference ΔE

$$\Delta E = E_{B,1} - E_{B,2} \ , \quad (2.56)$$

which either ionizes a third electron (Auger electron) from an orbital at a higher energy $-E_{B,3}$ or is emitted as a photon in an alternative process named x-ray fluorescence. The kinetic energy of the Auger electron is given by

$$E_{kin} = (E_{B,1} - E_{B,2}) - E_{B,3} - \Phi \ , \quad (2.57)$$

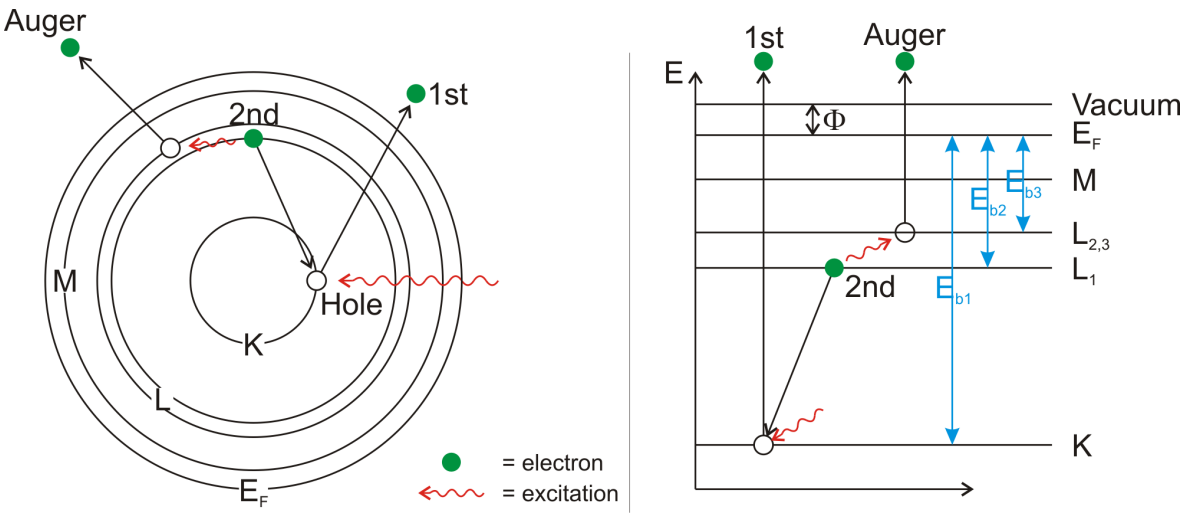

Figure 2.12: Schematic sketch of the auger effect for a KLL Auger electron from a spatial (left) and an energetic (right) point of view.

where Φ is the work function (i.e. the energy difference between Fermi and vacuum energy). The nomenclature of an Auger electron is given by the letters corresponding to the electron shells of the three electrons taking part in its emission process (in order). This means for an Auger process in which the first electron is ionized from the K shell, the second electron originates from the L shell and the third (auger) electron is emitted from the L shell, the auger electron is labeled as an KLL electron, see Figure 2.12.

Auger electrons exhibit electron energies in the energy range 10eV $\leq E_{kin} \leq$ 2000eV. Due to the IMFP of electrons in this energy regime $IMFP \approx 10$ Å (cf. Figure 2.8), the collection and interpretation of Auger electrons spectra ($\equiv$ Auger electron spectroscopy [AES]) is a very surface sensitive technique. Due to the origin of the Auger electrons their energies are element specific allowing for an identification of the elements in/on a sample (e.g., for the confirmation of its cleanness). What is more, by comparison of intensities the stoichiometry can be determined [14].

3 Investigated materials and systems

In this chapter the basic properties of the material systems (investigated in this thesis) necessary to understand the interpretation of the experiments performed are discussed.

3.1 Silicon

Silicon is the element with the symbol Si and the atomic number 14. It is part of the carbon group and exhibits the electronic configuration [Ne] $3s^2$ $3p^2$. Due to the fact that it is a semi-conductor, its conductivity can easily be tuned by doping with other elements (e.g. gallium and arsenic) and due to the fact that it is fairly inexpensive (compared to other semi-conductors), it is the predominantly used substrate in microelectronic applications. It crystallizes in a face-centered cubic lattice with a two atomic basis (diamond cubic structure, see Figure 3.1) with a lattice constant $a_{Si} = 5.4310$ Å and a melting temperature $T = 1410°C$. Due to the fact that all Si atoms are sp^3 hybridized in the crystal, all atoms exhibit a tetrahedral bonding configuration with a nearest-neighbor distance $a_{NN} = 2.3517$ Å.

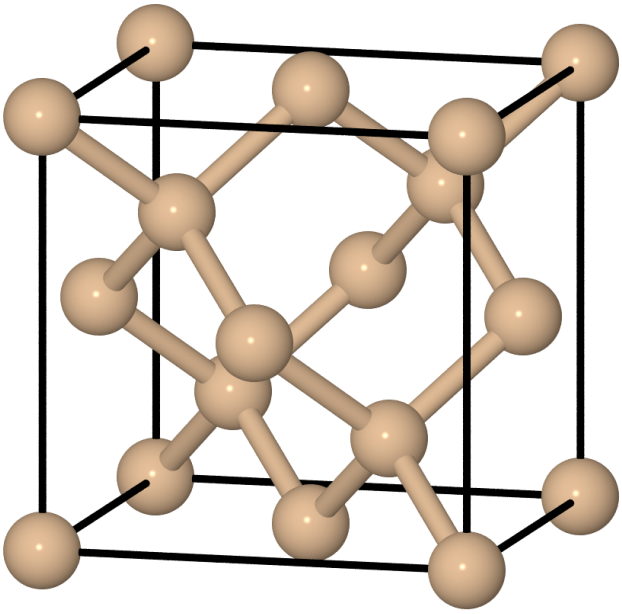

Figure 3.1: Sketch of the bulk silicon crystal structure (diamond cubic structure) showcasing the tetrahedral bonding of Si atoms to one another.

3.1.1 The Si(001) surface

The unreconstructed Si(001) surface, see Figure 3.2(a), exhibits a quadratic surface structure with the lattice constant $a_{001} = a_{Si}/\sqrt{2} = 3.8403$ Å and the layer-spacing $d_{001} = a_{Si}/4 = 1.3578$ Å. It contains two unsaturated bonds per surface Si-atom making it energetically unfavorable. Upon annealing it reconstructs into a (2×1) superstructure, see 3.2(b), by

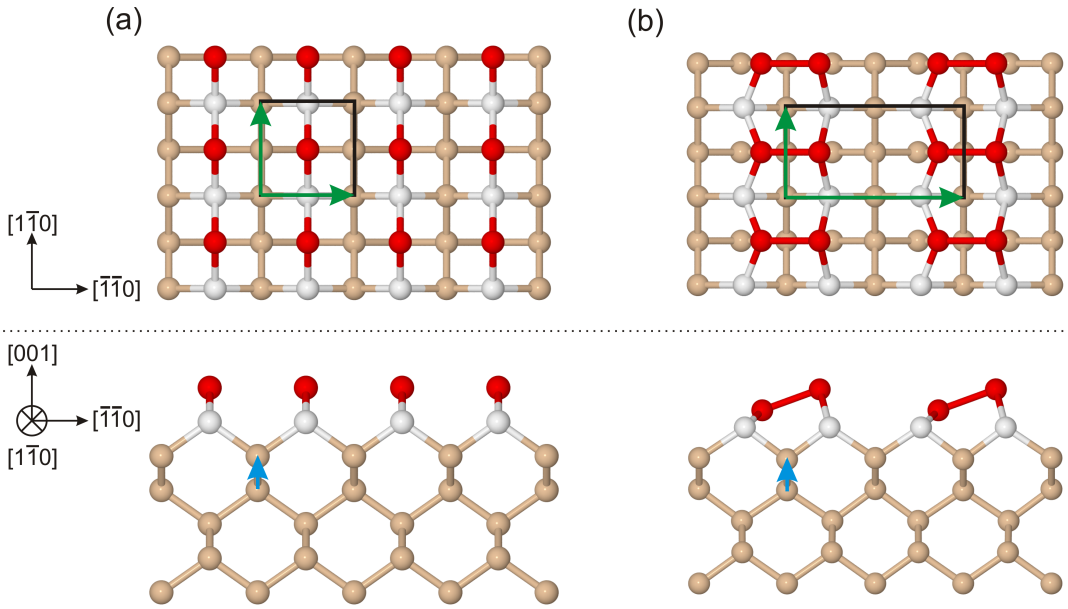

Figure 3.2: (a) Crystal structure of the unreconstructed Si(001) surface and (b) crystal structure of the (2×1)-reconstructed Si(001) surface (showing only one of the two possible dimer orientations). [unit cells (black boxes), crystallographic vectors (green arrows), layer-spacing (blue arrow), topmost Si layer (red atoms), second Si layer (white), lower Si layers (brown)]

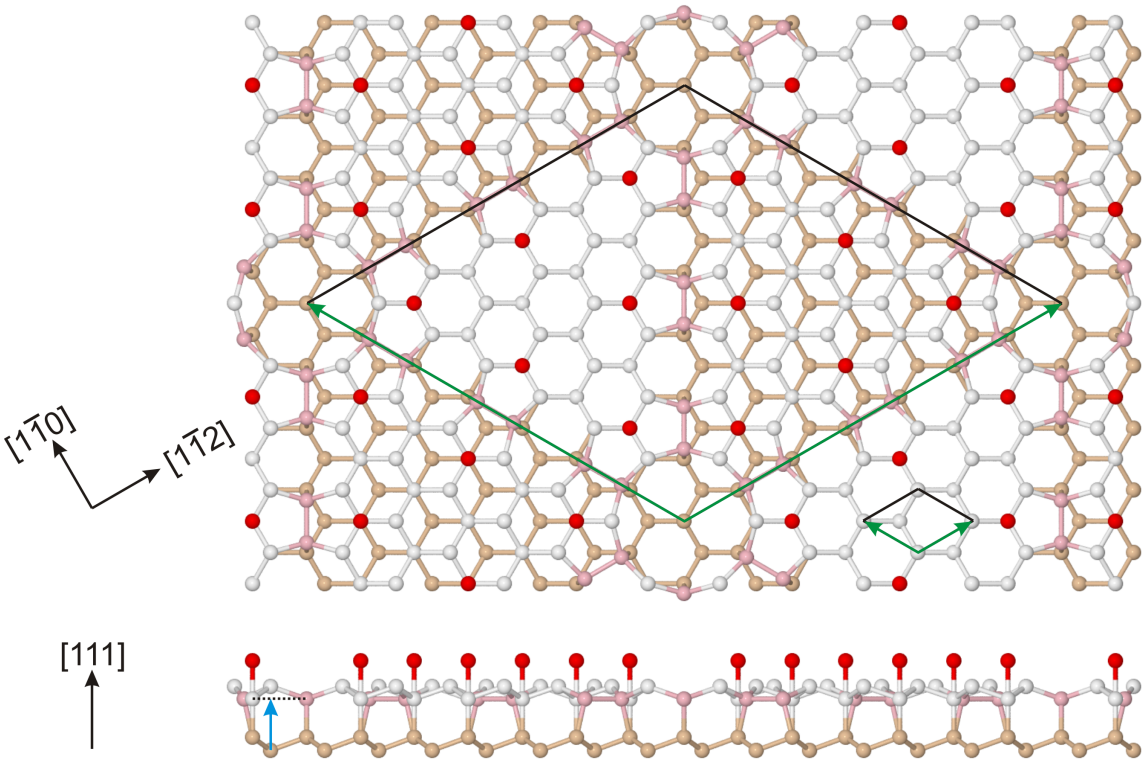

Figure 3.3: Crystal structure of the (7 × 7) reconstructed Si(111) surface. Additionally, one remaining unreconstructed (1 × 1) unit cell (inside the (7 × 7) reconstruction) is highlighted. [unit cells (black boxes), crystallographic vectors (green arrows), layer-spacing (blue arrow), adatoms (red atoms), dimer atoms (pink), top two Si layers (white), lower Si layers (brown)]

dimerization of the topmost Si atoms reducing the number of unsaturated bonds by half. The dimers are asymmetric, however, they can be tilted in two different directions due to the symmetry of the surface. At room temperature these dimers flip between both orientations at such a high rate that they become indistinguishable. Only for lower temperatures (T $\leq$ 200K [26]) the dimer orientations can be resolved and the (2 × 1) superstructure transforms into a c(2 × 4) reconstruction.

3.1.2 The Si(111) surface

The unreconstructed Si(111) surface exhibits a hexagonal surface structure with the lattice constant $a_{111} = a_{Si}/\sqrt{2} = 3.8403$ Å and the layer-spacing $d_{111} = a_{Si}/\sqrt{3} = 3.135$ Å, see Figure 3.3 (small unit cell). Due to the fact that it contains one unsaturated bond for each surface Si-atom it is metastable only. Upon cleavage under ultra high vacuum (UHV) conditions the

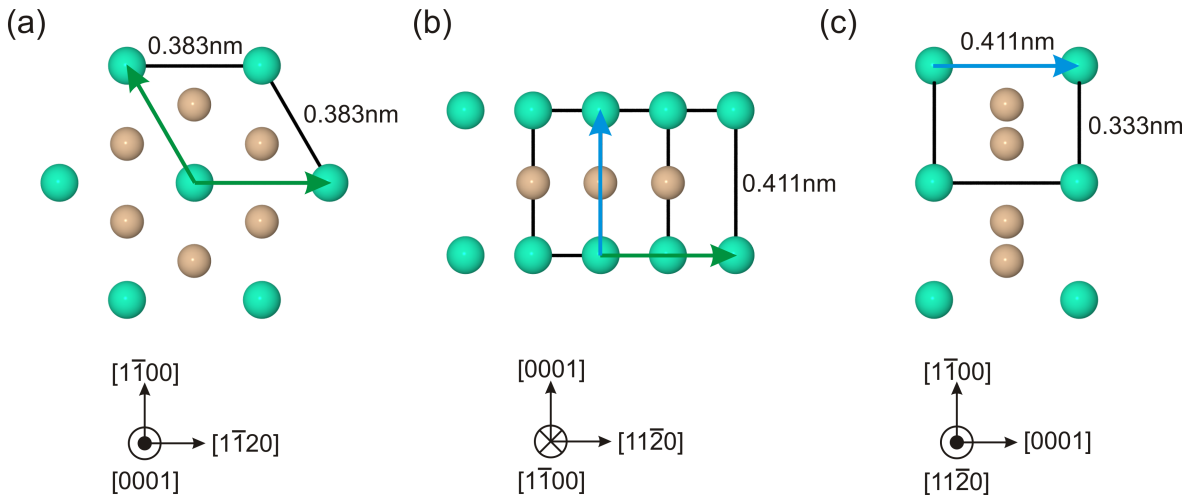

Figure 3.4: (a)-(c) Three slices through the bulk crystal structure of the Dy-silicide $DySi_2$. [unit cell (black boxes), crystallographic vectors a (green arrows), crystallographic vector c (blue arrows), Si (brown), Dy (turquoise)]

(2×1) reconstruction is formed which is metastable as well. Both surfaces are converted to the stable (7×7) reconstruction upon annealing, see Figure 3.3 (large unit cell), described by the so-called DAS-model (dimer-adatom-stacking-fault [27]), reducing the number of unsaturated bonds (7×7) per unit cell from 49 to 19 (as compared to the unreconstructed surface). Due to the high complexity of the (7×7) reconstruction it is not possible to obtain it from a contaminated surface. Consequently, obtaining the (7×7) reconstruction is a benchmark test for a clean surface.

3.2 Dysprosium

Dysprosium is the element with the symbol Dy and the atomic number 66. It exhibits the electronic configuration $[Xe]4f^{10}6s^2$ and is part of the lanthanides (atomic number 57-71) which are part of the rare-earth elements. It crystallizes in a hexagonal crystal structure with a melting temperature of $T = 1407°C$. It is a base metal and consequently shows a high reactivity. In compounds it is commonly found as a trivalent cation. Rare-earth elements and lanthanides exhibit a similar chemical character due to the fact that the only difference in electronic structure takes place in an inner shell (f-shell).

3.2.1 Dysprosium on Si(111)

Exposing Si(111) to Dy at elevated temperatures (400°C-700°C) either leads to the formation of Dy-induced reconstructions (in the sub-monolayer regime) or reconstructions based on the bulk Dysprosium silicide structure $DySi_2$, see Figure 3.4(a)-(c) (in the monolayer to multilayer regime).
In the sub-monolayer regime the (5×2)- and the $(2\sqrt{3} \times 2\sqrt{3})R30°$-reconstruction can be

observed [28, 29, 30, 31, 32, 33, 34]. Here, the Dy-atoms adsorb on top of the Si(111) surface and do not penetrate it (hence, it is referred to as a Dy-induced reconstruction).
In contrast to this, for the monolayer to multilayer regime the Dy-atoms penetrate the Si(111) surface forming the (1×1)-reconstruction for a single monolayer and the $(\sqrt{3} \times \sqrt{3})$R30°-reconstruction for multilayers both of which are based on the bulk structure of the Dy-silicide $DySi_2$ [28, 32, 33, 34, 35, 36], see Figure 3.5. For both reconstructions the $[0001]_{DySi_2}$ direction of the bulk Dy-silicide is orientated parallel to the $[111]_{Si}$ direction of the Si surface (i.e. the Si(111) surface normal is parallel to the surface normal of the crystal slice in Figure 3.4(a)). Additionally, the $[1\bar{1}00]_{DySi_2}$- is parallel to the $[1\bar{1}0]_{Si}$-direction and the $[11\bar{2}0]_{DySi_2}$- to the $[11\bar{2}]_{Si}$-direction meaning that the crystallographic axes of the bulk Dy-silicide and the Si(111) surface coincide. Due to the small in-plane lattice misfit (less than 1%) the Dy silicide grows epitaxially on the Si(111) surface.

The (1×1)-reconstruction consists of one subsurface Dy-layer which is sandwiched between two Si(111) (bulk-like) bi-layers with the same orientation thus exhibiting a $DySi_2$ stoichiometry. In contrast to this, the multilayer $(\sqrt{3} \times \sqrt{3})$R30°-reconstruction exhibits multiple (at least two) Dy subsurface layers. Here, the topmost layer is analogous to the topmost layer of the (1×1)-reconstruction, however, for the deeper (subsurface) layers of the reconstruction there are no Si bi-layers present. Instead, the Si atoms are arranged silicene-like in these layers (meaning that all Si atoms exhibit the same height). Additionally, a periodic Si vacancy network is induced in the subsurface layers. For the $(\sqrt{3} \times \sqrt{3})$R30°-reconstruction there is one vacancy per $(\sqrt{3} \times \sqrt{3})$R30°-unit cell equating to a nominal stoichiometry of Dy_3Si_5. However, depending on the sample preparation the density of Si vacancies can be reduced to half (consequently exhibiting a $(2\sqrt{3} \times \sqrt{3})$R30°-periodicity, see Figure 3.6) inducing a unidirectional strain in the silicene-like layers. This strain is compensated by (anti-phase) domain boundaries separating domains in one crystallographic direction thus forming quasi-one-dimensional domains (cf. chapters 5 and 6).

3.2.2 Dysprosium on Si(001)

Exposing Si(001) to Dy at elevated temperatures (400°C-700°C) either leads to the formation of Dy-induced reconstructions (in the sub-monolayer regime) or reconstructions based on the bulk Dysprosium silicide structure $DySi_2$, see Figure 3.4(a)-(c) (in the sub-monolayer to multilayer regime).
For low coverages (≤ 0.5 monolayers) the Dy-induced (2×4)-reconstruction and the (2×7)-reconstruction can be observed, see Figure 3.7.

For higher coverages (≥ 0.5 monolayers to multilayers) so-called nanowires (structural motifs with a very high aspect ratio) can be found whose structure is based on the bulk Dy-silicide structure $DySi_2$ (cf. Figure 3.4(a)-(c)).
For low Dy coverages the structure of the surface is proposed to consist of a Si(001) surface where the Si-dimers are replaced by Dy atoms forming the (2×4)-reconstruction containing three Dy atoms per unit cell ($\equiv 0.375$ monolayers) [37]. Increasing the coverage the (2×7)-reconstruction emerges (which is observed simultaneously with the (2×4)-reconstruction) which itself consists of sub-units with a (2×4)-periodicity (with a structure similar to the

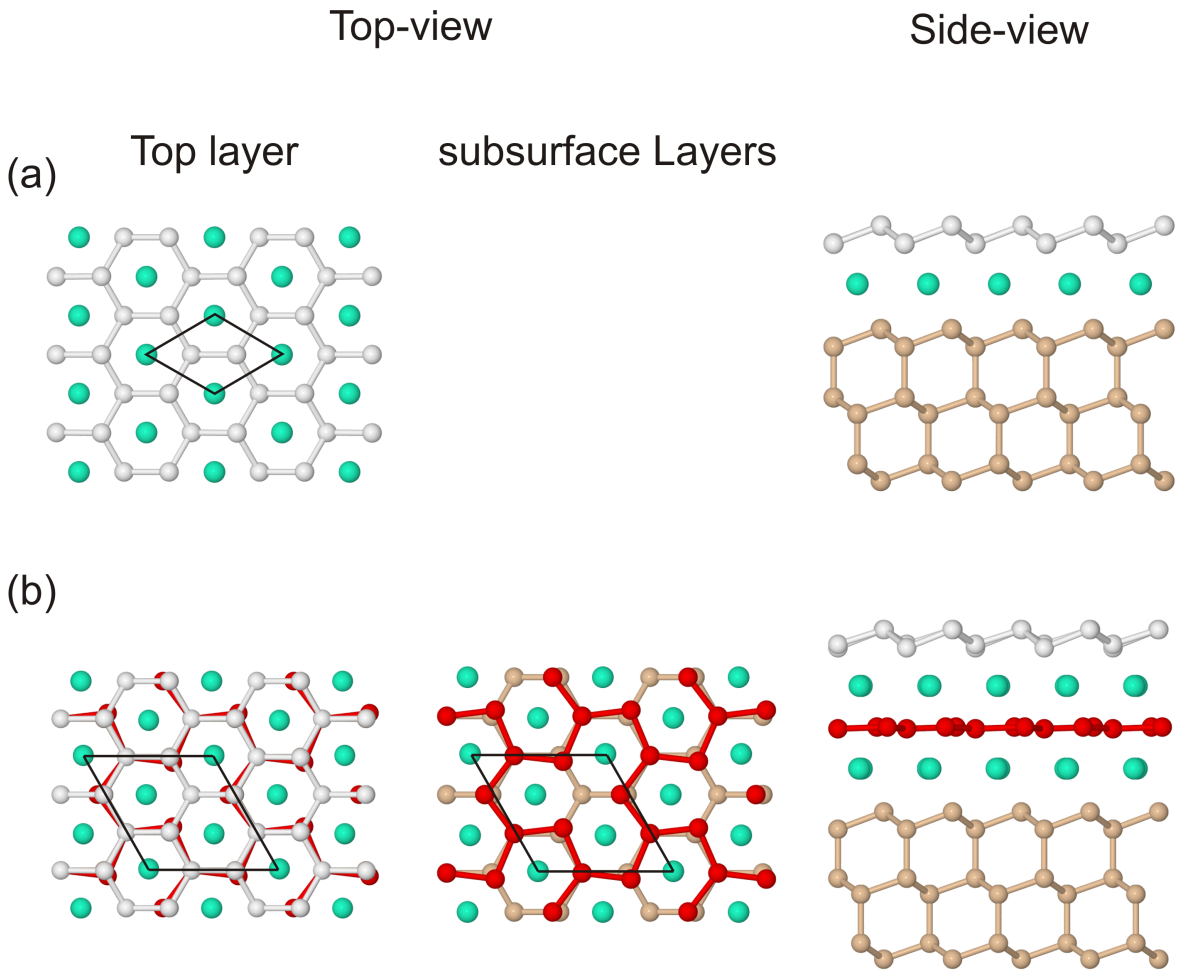

Figure 3.5: Crystal structure of the (1×1)-reconstruction (a) and the $(\sqrt{3} \times \sqrt{3})$R30°-reconstruction (b) observed on Si(111) for Dy exposure in the monolayer to multilayer regime. Coordinates taken from [34]. [Dy (turquoise), bulk Si(111) (brown), surface Si (white), subsurface Si (red)].

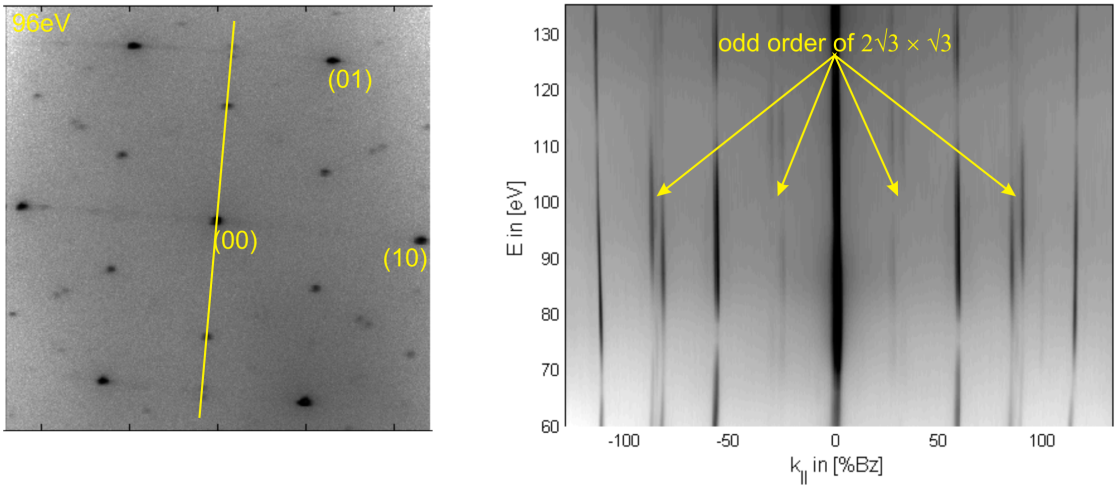

Figure 3.6: (a) Diffraction pattern of the $(2\sqrt{3} \times \sqrt{3})$R30°-reconstruction exhibiting a splitting of some diffraction spots characteristic for the arrangement in quasi-one-dimensional domains. (b) Diffraction pattern along the yellow line in (a) (recorded at different energies) showing an energy dependence of the odd-order diffraction peaks of the $(2\sqrt{3} \times \sqrt{3})$R30°-reconstruction (yellow arrows).

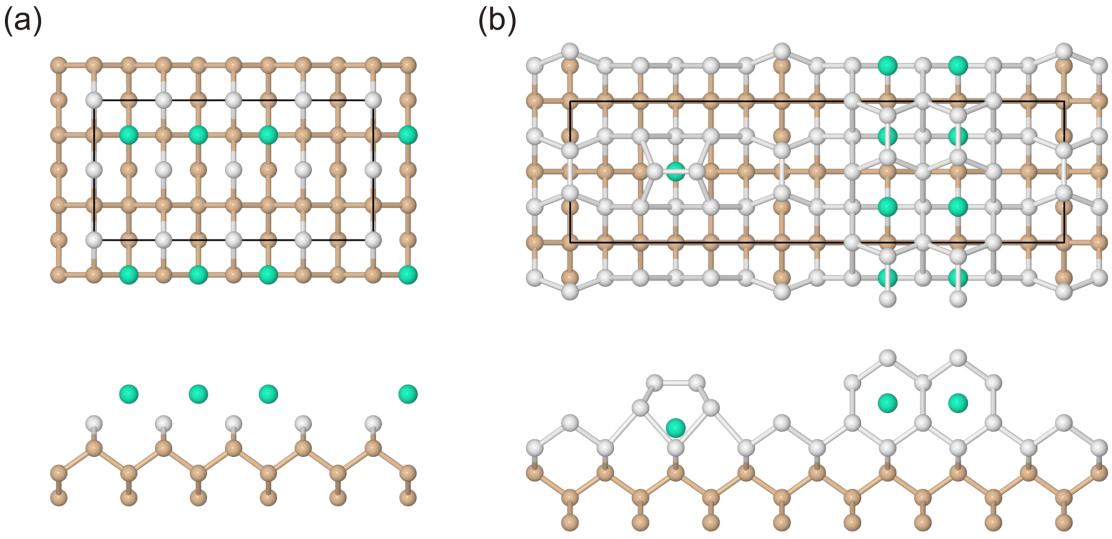

Figure 3.7: (a) Proposed crystal structure for the (2×4)-reconstruction. Coordinates taken from [37]. (b) Proposed crystal structure for the (2×7)-reconstruction. Coordinates taken from [38]. [unit cell (black boxes), surface Si atoms (white), bulk-like Si (brown), Dy (turquoise)]

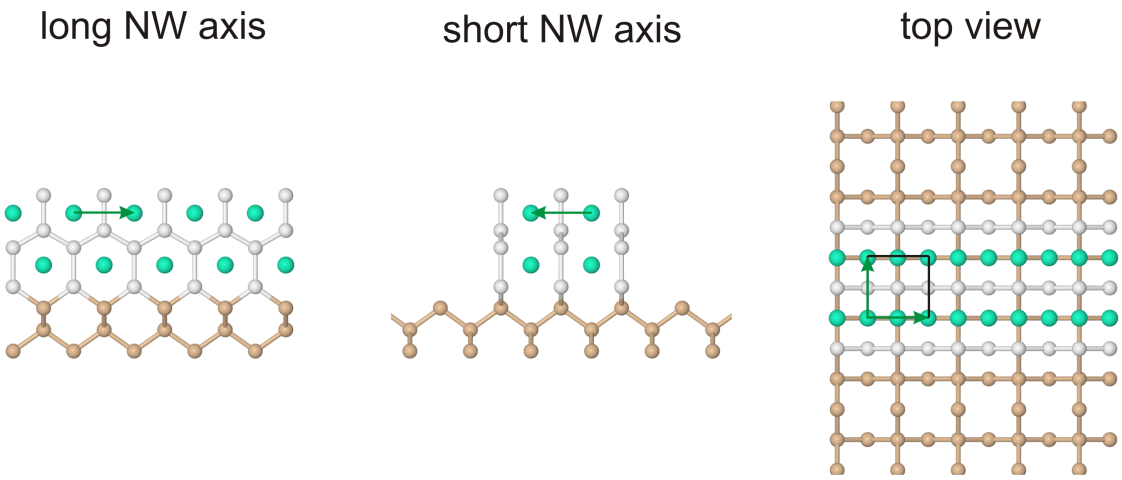

Figure 3.8: Proposed crystal structure for the Dy-silicide NWs growing on the Si(001) surface (here for a NW with a width of two lattice units). The NWs exhibit large aspect ratios due to an anisotropic lattice misfit. Coordinates taken from [10]. [unit cell (black boxes), crystallographic vectors (green arrows), Si in NWs (white), bulk-like Si (brown), Dy (turquoise)]

(2 × 4)-reconstruction) and a (2 × 3)-periodicity containing six atoms in total (≈ 0.429 monolayers) which functions as a wetting layer for the nanowire growth [9, 38, 39].

As already mentioned, the structure of the nanowires, see Figure 3.8, is based on the bulk Dy-silicide structure $DySi_2$. In contrast to the Si(111) surface, however, the growth orientation is different. On the Si(001) surface the $[1\bar{1}00]_{DySi_2}$-direction grows parallel to the $[001]_{Si}$-direction. Additionally, the $[0001]_{DySi_2}$ is parallel to the $[1\bar{1}0]_{Si}$ direction and the $[11\bar{2}0]_{DySi_2}$ direction to the $[\bar{1}\bar{1}0]_{Si}$ direction (or vice-versa due to the cubic symmetry of the Si(001) surface). The lattice constants of the $DySi_2$ structure are different in $[0001]_{DySi_2}$- and $[11\bar{2}0]_{DySi_2}$-direction (4.11 Å and 3.83 Å, respectively), consequently, the structure is subject to lattice mismatches of different magnitude (-0.3% and 7.3%, respectively). Hence, the structure grows epitaxially alongside the direction with the small lattice misfit (NW-lengths in the μm regime) whereas it is limited to several unit cells in the other direction (NW-widths of 2-16 lattice units) explaining the formation of nanowire-like structures (with large aspect ratios) [10].

For very low coverages (≤0.21 monolayers) only the (2 × 4)-reconstruction can be observed, see Figure 3.9. Further increasing the Dy coverage (∼0.21 - 0.63 monolayers), the (2 × 7)-reconstruction emerges as well. For lower temperatures ($T \sim 500°C$) the (2 × 7)-reconstruction cannot be prepared exclusively whereas for higher temperatures ($T \sim 600°C$) this is possible (for ∼0.42 monolayers). Increasing the Dy coverage further leads to a decrease of the (2 × 7)-reconstruction due to the formation of nanowires. For even higher Dy coverages (≥ 0.63 - 1.05 monolayers) the (2 × 7)-reconstruction vanishes completely and only nanowires and the (2 × 4)-reconstruction (at $T \sim 600°C$) can be observed. For the highest

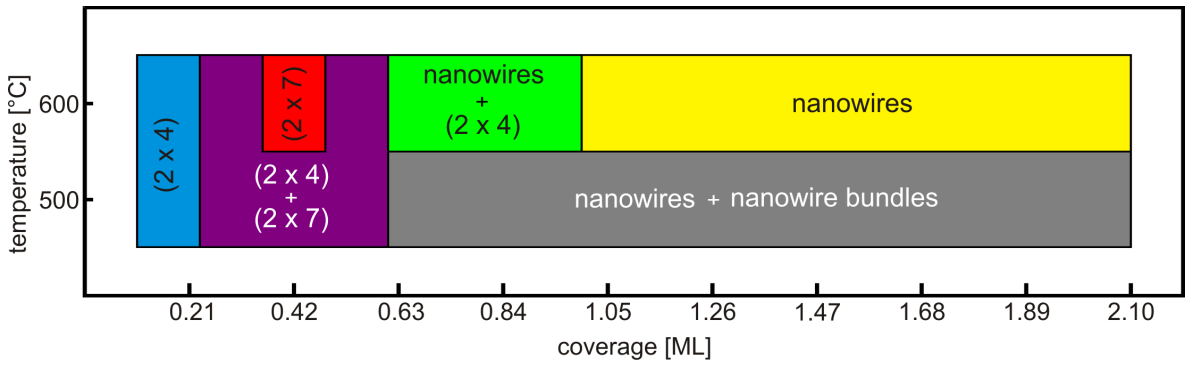

Figure 3.9: Submonolayer to monolayer phasediagram of the Dy/Si001-system. Taken and adapted from [40].

coverage regime ($\geq$ 1.05 monolayers) nanowire bundles start to form [10] until (basically) the whole surface is covered by nanowire bundles ($\sim$ 2.1 monolayers) for temperatures $T \sim 500$°C whereas basically no bundling is observed for higher temperatures $T \sim 600$°C.
Inside the bundles adjacent nanowires (of different width) are separated by a distance of one Si(001) lattice unit. The distance between bundles, however, is critically determined by the Dy coverage (cf. chapter 7). On top of the nanowires different reconstructions have been reported, namely (1 $\times$ 1)-, (2 $\times$ 1)- and c(2 $\times$ 2)-reconstructions by Liu et al. [10] and a (2 $\times$ 1)-reconstruction by Preinesberger et al. [41]. Here, LEED experiments favor the (1 $\times$ 1)-reconstruction (cf. chapter 7).
For Dy coverages exceeding 2.1 monolayers three dimensional island growth is observed.

3.3 Gold

Gold is the element with the symbol Au and the atomic number 79. It exhibits the electronic configuration [Xe]$4f^{14}5d^{10}6s^{1}$ and crystallizes in a face-centered cubic crystal structure with a melting temperature $T = 1064$°C. It usually assumes the oxidation states 0, +I or +III in compounds, however, due to the fact that it is a noble metal it shows a low reactivity and does not form compounds with many elements.

3.3.1 Gold on Si(111)

Exposing the Si(111) surface to Au at elevated temperatures (400°C-800°C) leads to the formation of Au-induced reconstructions in the submonolayer to monolayer regime, see Figure 3.10. For low coverages the surface retains its (7 $\times$ 7)-periodicity (which now is essentially given by the well-known (7 $\times$ 7)-reconstruction decorated with Au adsorbates). For higher coverages of 0.6 - 0.7 monolayers a (5 $\times$ 2)-reconstruction can be observed. For even higher coverages (1 monolayer) the $(\sqrt{3} \times \sqrt{3})$- and ($\geq$ 1 monolayer) the (6 $\times$ 6)-reconstruction can be observed which are both based on a structural motif with $(\sqrt{3} \times \sqrt{3})$-periodicity and gradually transition from one to the other in a disorder to order transition [42].

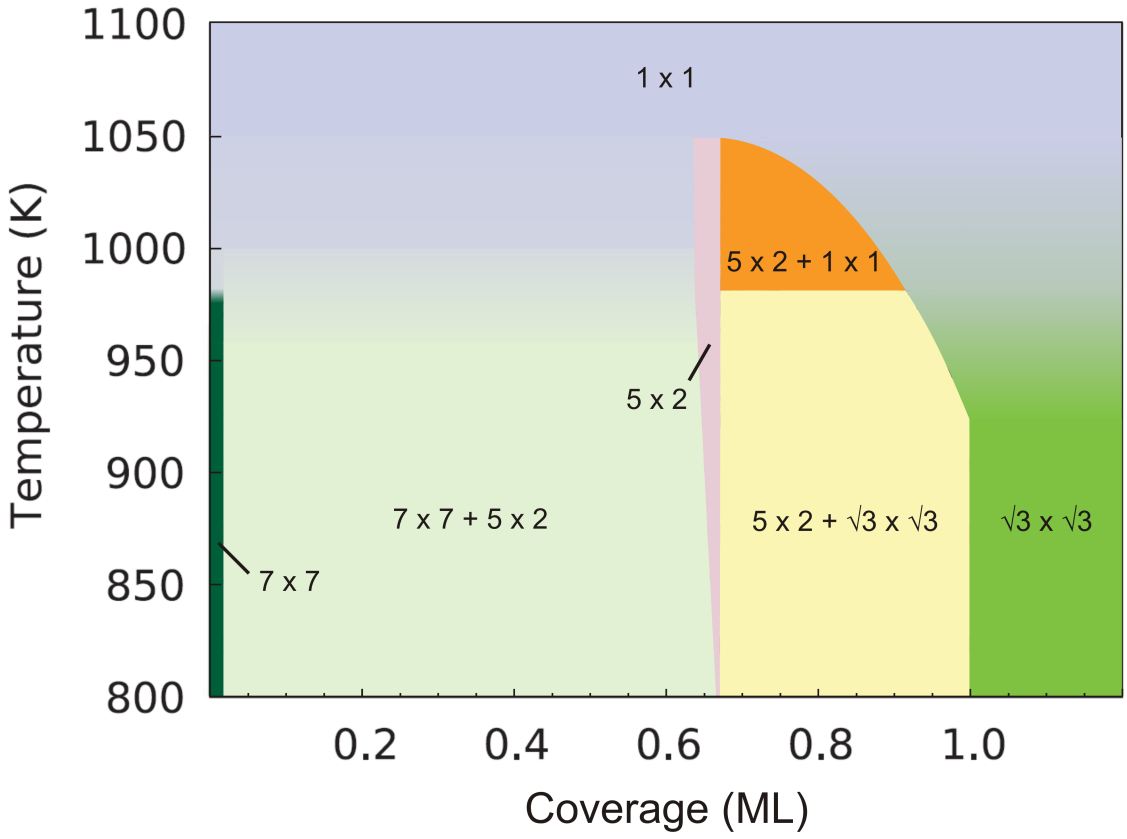

Figure 3.10: Submonolayer phasediagram of the Au/Si(111)-system. Taken and adapted from [43].

Additionally, it should be noted here, that the (5×2)-reconstruction can occur simultaneously with its adjacent phases (the (7×7)- for lower and the $\left(\sqrt{3} \times \sqrt{3}\right)$-reconstruction for higher coverages) depending on the actual coverage and preparation parameters. For high temperatures ($T \geq 1050$K) both the (5×2)-reconstruction and the $\left(\sqrt{3} \times \sqrt{3}\right)$-reconstruction transform into a disordered (1×1)-phase.

4 Experimental setup

4.1 UHV chamber

Figure 4.1 shows the schematic setup of the UHV-chamber in which (most of) the samples investigated in this thesis were prepared. It is equipped with a SPA-LEED device, an AES device, an Evaporator, a rotary manipulator, a load-lock system and a transfer system to transfer the sample from the load-lock to the UHV-chamber and vice-versa enabling the exchange of samples without breaking the vacuum in the UHV-chamber.
The base pressure inside the chamber (p = 1×10^{-10} mbar) is achieved through the combination of four different type of pumps, namely a rotary vane pump, a turbomolecular pump, an ion getter pump and a titanium sublimation pump (for further information on the function and the interplay of these pumps the reader is relegated to [14]). It is possible to heat the sample via direct current heating enabling sample temperatures of T $\geq$ 1200°C. The temperature of the sample is determined by measuring its infrared radiation via an infrared pyrometer through the window of the chamber.

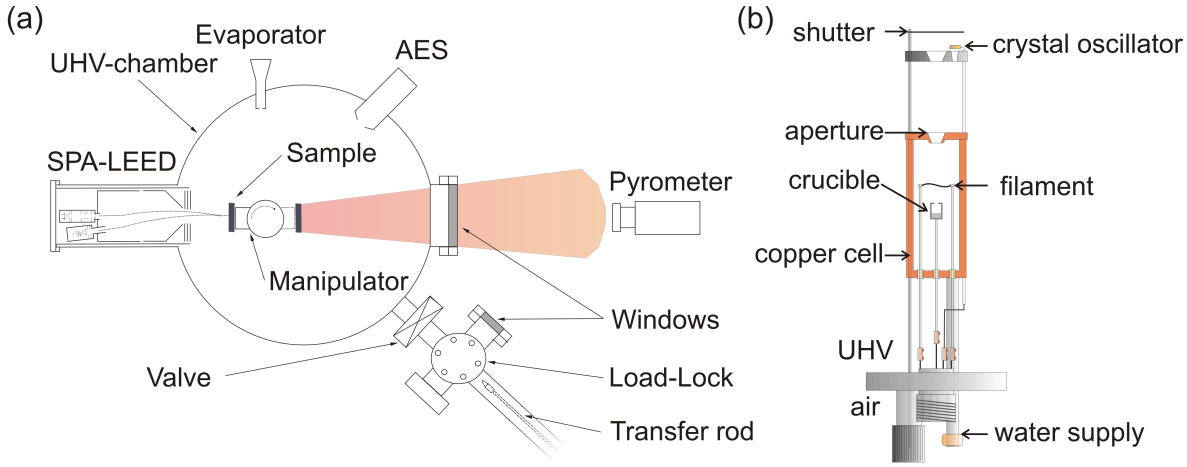

Figure 4.1: (a) Schematic display of the UHV-chamber. The lines going out of the SPA-LEED instrument to the sample correspond to the trajectory of electrons in a diffraction experiment and the colored area to the infrared radiation emitted by the sample. Taken and modified from [44]. (b) Schematic sketch of an evaporator equipped with a crucible in which the materials to be evaporated are stored. Taken and modified from [45].

4.2 Sample preparation

The Si substrates are cut from a silicon wafer to match the size of the sample holder of the UHV-chamber. Subsequently, they are cleaned with aceton, isopropanol and water to remove adsorbates. After the transfer to the UHV-chamber they are degassed for 12 hours at 600°C by direct current heating (in order to remove the remaining adsorbates) until the base pressure is smaller than $p = 2 \times 10^{-10}$ mbar. Thereafter the substrate is treated by

a method called flash-annealing to remove the native Si-oxide. Flash-annealing consists of several heating cycles (≈ 10) in which the starting substrate temperature (600°C) is increased close to its melting temperature (1200°C) nearly instantaneously then is held there for several seconds ($\approx$ 10s) before it is decreased to the starting temperature again (about as fast as it was increased). Additionally, the pressure needs to be monitored during the heating cycles and may not exceed $p = 2 \times 10^{-9}$ mbar in order to prevent contamination of the surface. After flash-annealing the sample SPA-LEED and AES experiments are performed to check the cleanliness of the substrate. Here, the observation of the well-known (7×7) or (2×1) reconstruction (for Si(111) and Si(001) respectively) in the diffraction pattern and an absence of contaminants in the AES spectra act as benchmark for a clean surface.

4.3 Evaporator

The materials brought onto the substrates in this thesis are deposited by means of physical vapor deposition. Figure 4.1(b) shows the schematic design of a evaporator used to do so. The material to be evaporated is placed in a crucible and a high voltage between the filament and the crucible is applied (where the crucible is on a positive potential compared to the filament). If a sufficiently high current is put through the filament the electrons emitted from it (by thermionic emission) are accelerated towards the crucible. Upon impinging on it the kinetic energy of the electrons is converted into heat heating up the crucible and the material which is contained in it. In order to confine the heating to the crucible only (thus keeping the increase in pressure at a minimum) the rest of the evaporator is cooled by water. If the temperature of the crucible exceeds the sublimation/boiling temperature of the material to be evaporated the material starts to sublimate/evaporate forming a molecular beam due to the shape of the crucible and the aperture of the evaporator. The amount of evaporated material can be assessed by the change in frequency of a crystal oscillator. Additionally, the evaporator is equipped with a shutter which can be closed to terminate the exposure of a sample to the evaporating material immediately. This enables the deposition of precise amounts of material onto a sample.

4.4 SPA-LEED

Figure 4.2 shows the schematic design of a SPA-LEED instrument. It consists of an electron gun emitting the electrons used for the diffraction (in the energy range from $0 \leq E \leq 500$eV), two octopoles controlling the trajectory of the emitted and diffracted electrons, a crystal lens focusing emitted and diffracted electrons onto and from the sample and a channeltron collecting the diffracted electrons. Opposed to conventional LEED measurements the angle of incidence ϵ of the electrons onto the sample is not constant for SPA-LEED experiments. Instead, it is varied during the experiment by means of applying varying voltages to the octopole plates, thus scanning the Ewald sphere (see Figure 4.3). Additionally, the electrons are not detected by a fluorescent screen but by a channeltron instead. Due to the fact that the electron gun and the electron detector (channeltron for SPA-LEED) are not aligned on the same axis (which is the case for the fluorescent screen and the electron gun for perpendicular

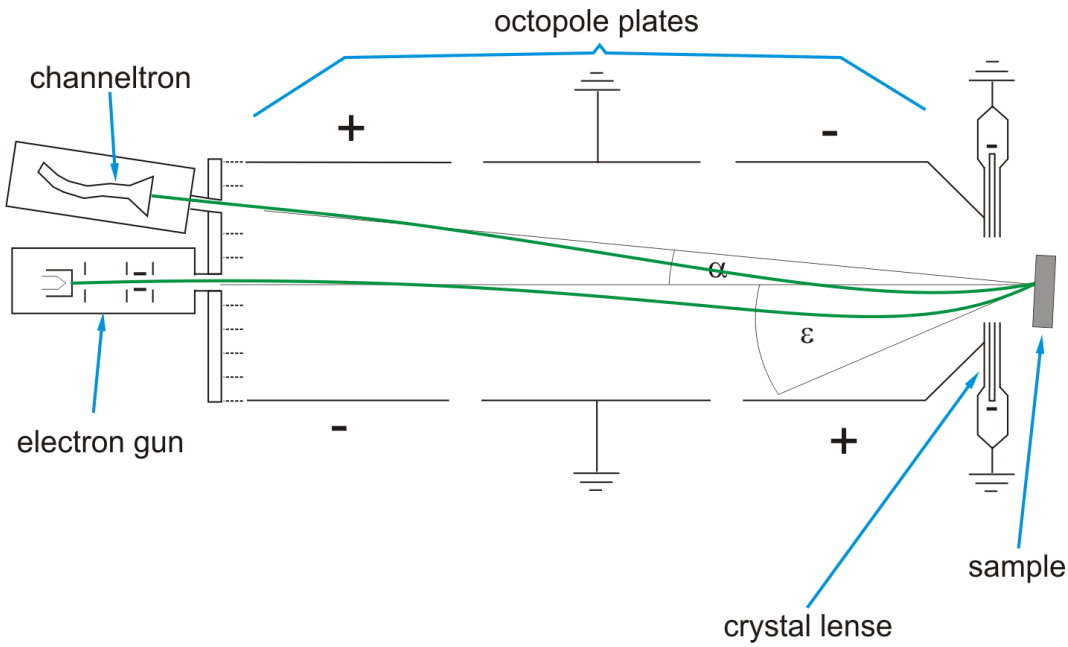

Figure 4.2: Schematic sketch of the SPA-LEED instrument. Taken and modified from [46].

incidence for conventional LEED) the specular reflection diffraction spot can be recorded. The angle α under which the diffracted electrons are detected is kept constant. Consequently, the radius of the Ewald sphere is twice as large for SPA-LEED (compared to conventional LEED) experiments and a larger fraction of the reciprocal space can be accessed (for the same electron energy). Due to the collection of electrons via a channeltron and the high degree of control over the angle of incidence ϵ via the octopole plates angular resolutions much higher than those achievable by the human eye (or a video system used to capture the screen) in a conventional LEED setting can be achieved. Consequently, spot profiles can be collected very precisely allowing for quantitative approaches to the processing of the collected data.

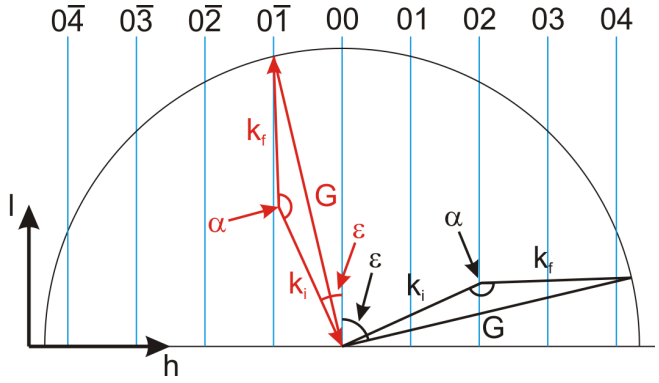

Figure 4.3: Ewald construction for the SPA-LEED experiment exemplifying the scanning of the Ewald sphere by means of two different diffraction conditions. Additionally, the lattice rods of the reciprocal lattice are displayed in blue.

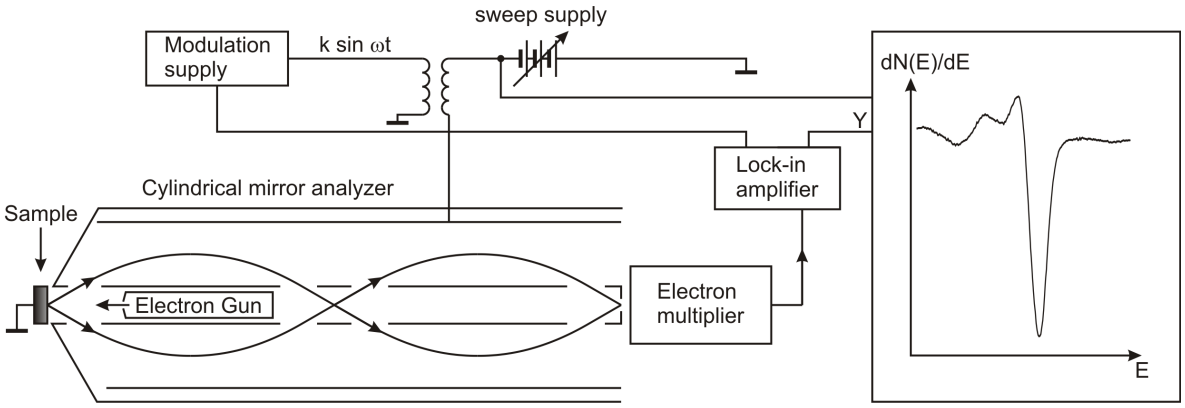

Figure 4.4: Schematic sketch of a typical AES setup. Taken and adapted from [14].

4.5 AES

Figure 4.4 shows a sketch of a typical AES setup. Electrons are emitted from an electron gun (3kV $\leq E \leq$ 5kV), impinge on the sample and induce (among other things) the emission of Auger electrons. These Auger electrons are emitted from the sample (cf. chapter 2.5) into a cylindrical mirror analyzer consisting of an inner and an outer cylinder. Due to an electrical field between these cylinders only electrons of a particular energy (which is scanned in the energy range $0 \leq E \leq$ 1000eV during an AES experiment) are able to pass through the analyzer and are detected by an electron multiplier. Due to the fact that the signal of the Auger electrons is small compared to the background (induced by inelastically scattered electrons) the electrical field between the cylinders is varied as a function of time ($\propto k \sin \omega t$ with a small amplitude k) and the intensity caused by the Auger electrons is retrieved using lock-in technology. Consequently, the signal is not given by the number of electrons detected but rather as the derivative (with respect to the energy) of this quantity instead.

4.6 SXRD-Experiments

The in-situ SXRD experiments were performed at the ID03 [47] and BM25 [48, 49] beamlines of the European Synchrotron Radiation Facility (ESRF) in Grenoble, France. Synchroton radiation has several advantages compared to conventional laboratory x-ray sources, e.g., high intensity, high brilliance and the possibility to tune the photon energy (in a fairly wide energy range). For further information on the generation and properties of synchrotron radiation the reader is referred to [50].

4.6.1 UHV chamber

The UHV setup can be equipped with evaporators in order to prepare a sample exhibiting the desired (adsorbate induced) surface structure. The successful preparation of the reconstructions can be assessed by LEED and x-ray photoelectron spectroscopy (BM25) and AES (ID03)

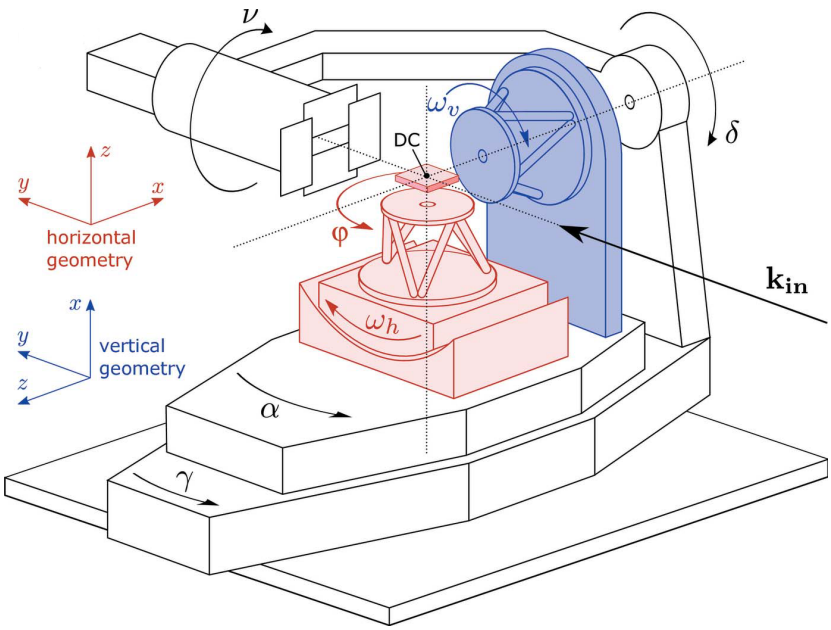

Figure 4.5: Schematical sketch of a 2S+3D diffractometer used at BM25 (without an UHV chamber) in the neutral position (all rotation angles are zero) showcasing the different rotation axes. The experiments in this thesis were performed in vertical geometry (with an UHV chamber mounted on the diffractometer). Taken and adapted from [51]

experiments prior to performing SXRD experiments. The UHV chamber itself is mounted on a 2S+3D diffractometer at the BM25 beamline, see Figure 4.5, and a six-circle diffractometer at the ID03 beamline enabling the execution of in-situ SXRD experiments without breaking UHV conditions.

4.6.2 SXRD

The interaction between x-ray radiation and matter is relatively weak (penetration depth of 100μm - 1000μm for photon energies of 10keV - 20keV for perpendicular incidence). Therefore, SXRD experiments are usually performed under a grazing angle of incidence α (which is chosen to be slightly larger than the critical angle (of total reflection, cf. chapter 2.4.1) to increase the surface sensitivity. What is more, the angle of incidence α is kept constant during the experiment. Consequently, the sample needs to be rotated about its surface normal ω in order to be able to access the complete reciprocal space (at a particular photon energy). Additionally, the (two-dimensional) x-ray single-photon-counting pixel detector [52] needs to be positioned in a direction, under the angles γ and δ, in which diffracted intensity I can be observed (due to the single crystalline nature of the samples intensity is observed only at certain spots/rods in reciprocal space, cf. Figure 4.6 for the Ewald construction).
During an actual SXRD experiment first a large number j of in-plane reflections I_j (h_j, k_j, l with ($l \sim 0$)) is collected (allowing for the generation of the Patterson function later on).

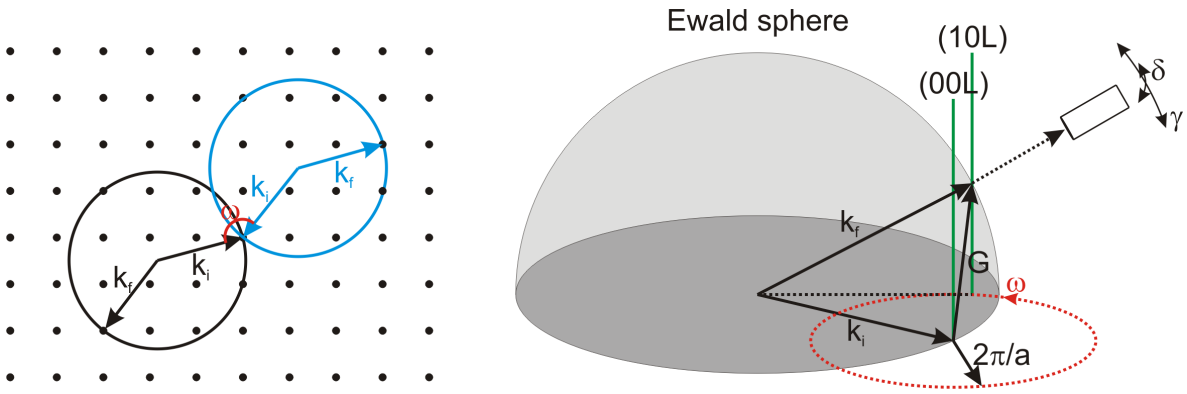

Figure 4.6: (a) Ewald construction for in-plane conditions ($l \sim 0$) showcasing that the sample has to be rotated about its surface normal (ω) to be able to record the bottom of all lattice rods (at a particular photon energy E). Taken and adapted from [14]. (b) Ewald construction for general conditions. In order to be able to record a particular lattice rod (h_n, k_n) at different out-of-plane conditions l_i (with $l_i \leq l_{max}(h_n, k_n)$) the sample has to be rotated about its surface normal (ω) and the detector has to be positioned in the direction of the diffracted wave (γ, δ). Taken and adapted from [53]

Afterwards, n lattice rods are recorded I_n (h_n, k_n, l_i with $0 \leq l_i \leq l_{max}(h_n, k_n)$) which can be used for the refinement of the atomic structure (cf. chapter 2.4).

Original publication: Phys. Rev. B. **94**, 205431 (2016)
available at https://doi.org/10.1103/PhysRevB.94.205431

Strain-induced quasi-one-dimensional rare-earth silicide structures on Si(111)

F. Timmer[*,**], R. Oelke[*,**], C. Dues[***], S. Sanna[***], W.G. Schmidt[***], M. Franz[****], S. Appelfeller[****], M. Dähne[****], J. Wollschläger[*,**]

[*] *Fachbereich Physik, Universität Osnabrück, Barbarastraße 7, 49069 Osnabrück, Germany*
[**] *Center of Physics and Chemistry of New Materials, Barbarastraße 7, 49069 Osnabrück, Germany*
[***] *Lehrstuhl für Theoretische Physik, Universität Paderborn, Warburgerstr. 100, 33095 Paderborn, Germany*
[****] *Institut für Festkörperphysik, Technische Universität Berlin, Hardenbergstraße 36, 10623 Berlin, Germany*

Original publication: Condens. Matter. B. **2**, 7 (2017)
available at `https://doi.org/10.3390/condmat2010007`

Effects of Domain Boundaries on the Diffraction Patterns of One-Dimensional Structures

F. Timmer[*,**], J. Wollschläger[*,**]

[*] *Fachbereich Physik, Universität Osnabrück, Barbarastraße 7, 49069 Osnabrück, Germany*
[**] *Center of Physics and Chemistry of New Materials, Barbarastraße 7, 49069 Osnabrück, Germany*

Original publication: J. Phys. Condens. Matter **29**, 435304 (2017)
available at https://doi.org/10.1088/1361-648X/aa8845

On the diffraction pattern of bundled rare-earth silicide Nanowires on Si(001)

F. Timmer*,**, J. Bahlmann*,**, J. Wollschläger*,**

* *Fachbereich Physik, Universität Osnabrück, Barbarastraße 7, 49069 Osnabrück, Germany*
** *Center of Physics and Chemistry of New Materials, Barbarastraße 7, 49069 Osnabrück, Germany*

Determination of the atomic structure of the Si(111)-(5×2)-Au-Reconstruction via Surface X-ray Diffraction

Abstract

By performing Surface X-ray Diffraction (SXRD) experiments and through the comparison of the experimentally collected in-plane diffraction data and the Patterson function derived from it with (calculated) Patterson functions derived from structure models proposed for the Si(111)-(5×2)-Au-Reconstruction in literature, i.e., the Abukawa-Nishigaya (AN), Erwin-Barke-Himpsel (EBH) and Kwon-Kang (KK) models we are able to rule out the AN model. Through the subsequent comparison of (computed) out-of-plane diffraction data of the EBH- and KK-models to the experimental out-of-plane diffraction data we are able to identify the most probable structure model as the KK-model. Additionally, we are able to refine the atomic structure of the KK-model by fitting the calculated out-of-plane diffraction data to the experimental one.

8.1 Introduction

The (5×2)-Au reconstruction on Si(111) has been in the focus of research for nearly 50 years now [3]. Lately, the interest has been spurred by the fact that the reconstruction can be regarded as a prototype of a self-assembled quasi-one-dimensional (1D) metallic chain structure [4, 5]. In order to understand the physical properties accompanying these 1D chains a profound knowledge of the atomic structure is needed. Historically a plethora of atomic structures containing 0.4 monolayers (ML) of Au were proposed, e.g. the initial Erwin model [54]. More recently, however, the Au coverage of the reconstruction has been revised twice, first to 0.6 ML [55] leading to the construction of the Erwin-Barke-Himpsel- (EBH [56]) and the Abukawa-Nishigaya-model (AN [57]) and then to 0.67 ML [43] leading to the Kwon-Kang-model (KK [58]) containing 0.7 ML Au, (cf. Figure 8.1). Most recently, Shirasawa et al. [59] performed Surface X-ray Diffraction (SXRD) experiments ruling out the AN-model, thus supporting the theoretical works of Hogan et al. [60] and the theoretical works of Seino et al. [61], while also favoring the KK-model over the EBH-model. In order to assess this result we also performed SXRD experiments.

8.2 Experimental

The SXRD experiments were conducted at the beamline BM25 of the European Synchrotron Radiation Facility (ESRF). The photon beam energy was 18 keV and the incidence angle 0.5°. The pressure inside the experimental chamber was lower than 5×10^{-10} mbar throughout the whole experiment. The Si(111) substrates were prepared by degassing for 12 h at 600°C and were flash-annealed at 1150°C several times afterwards until the well-known (7×7) reconstruction was observed in LEED. Au was deposited by means of physical vapor deposition from a molybdenum crucible on the clean 7×7 reconstructed Si(111) surface at room temperature . Subsequently, the sample was annealed post deposition at 800°C in several steps, checking the surface structure by LEED between heating steps, until only the desired 5×2 reconstruction was observable (cf. phase diagram in chapter 3.3.1 Figure 3.10). The crystallographic coordinate system used is given by $a = b = 3.8403$ Å, $c = 9.4068$ Å, $\alpha = \beta = 90°$

and $\gamma = 120°$ where a and b are the in-plane lattice constants and c is the out-of-plane lattice constant. Consequently, the scattering vector q can be given in relative lattice units (H, K, L) which are related to the reciprocal lattice via

$$\mathbf{q} = \mathbf{G} = H\mathbf{a^*} + K\mathbf{b^*} + L\mathbf{c^*} \ . \tag{8.1}$$

Planar Si(111)-wafers were used, consequently three rotational domains could be observed. In total, 35 in-plane reflections (L = 0.5) from the three rotational domains were measured, which equate to 18 symmetry-inequivalent reflections. Additionally 13 lattice rods ($1.5 \leq \mathrm{L} \leq 5$) were recorded, eight of which are symmetry-inequivalent. Due to the fact that the unit cells are not well aligned along the × 2 direction (random shifts of 1 lattice unit [62, 63]) no half-order diffraction spots for

$$K = 1/2 + n \quad \text{with} \quad n \in \mathbb{Z} \tag{8.2}$$

can be observed and only streaked intensity can be observed for

$$-\infty \leq H \leq \infty \tag{8.3}$$

instead. Consequently, reflections and lattice rods can only be collected for integer-order spots (in K). Additionally, all recorded reflections and lattice rods belong to the superstructure only (i.e. $H \neq \mathbb{Z} \equiv$ no crystal truncation rods) and therefore reflect only the structure of the superstructure.

8.3 Results and discussion

8.3.1 In-plane

The Patterson function P is given by

$$P(U,V,W) = \sum_{j}^{N} |F(H_j, K_j, L_j)|^2 \, e^{-2\pi i(H_j U + K_j V + L_j W)} \ , \tag{8.4}$$

where F is the (experimental) structure factor at the position [H_j, K_j, L_j] in reciprocal space, which is equivalent to the self-convolution of the electron density and thus contains information about the inter-atomic distances inside the unit cell. Additionally, the intensity observed in the Patterson function is proportional to the product of the atomic numbers Z of the atoms (i.e., Z(Si) and Z(Au)) which cause this intensity. The large discrepancy in atomic number between Z(Si) = 14 and Z(Au) = 79 means that the Patterson function primarily images Au-Au- and Au-Si-distances whereas Si-Si-distances only play a minor part.

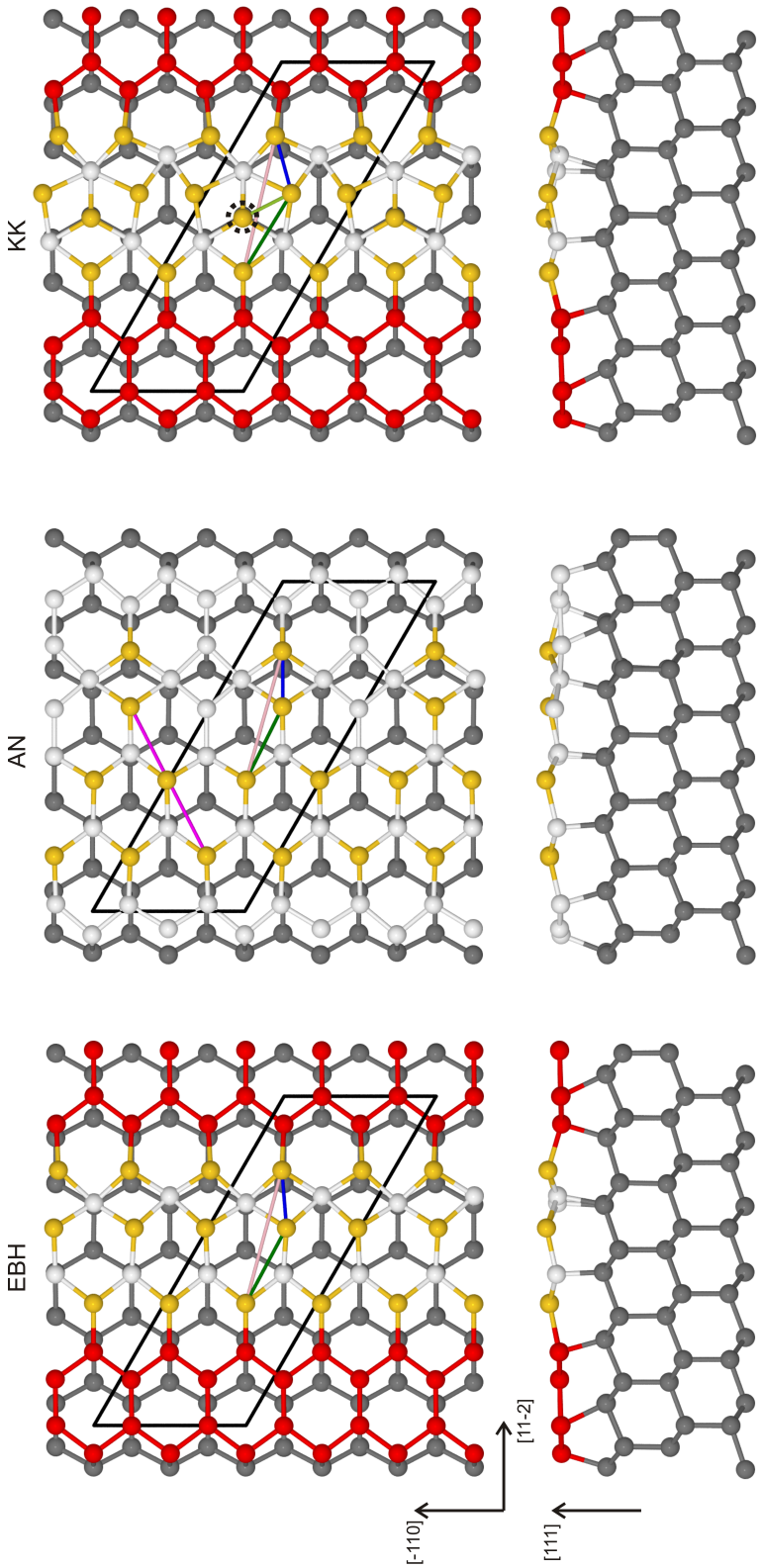

Figure 8.1: Schematic display of the three atomic structures of the 5 × 2 reconstruction proposed in literature lately (EBH [56], AN [57], KK [58]) omitting the Si adatoms. This is warranted by the fact that their distribution on the surface is random and consequently their influence on the diffraction pattern is very low. The EBH- and the AN-model have a Au-coverage of 0.6 monolayers (≡ 6 atoms per unit cell) whereas the KK-model exhibits an additional Au atom per unit cell (dashed black circle). The Au atoms in the AN-model form a structural motif resembling an "Eiffel tower" whereas the EBH- and the KK-model exhibit rows of Au atoms accompanied by a honeycomb shaped Si ring. Au atoms are displayed in gold, Si atoms in the topmost layer in white unless they are part of honeycomb ring (red) and Si atoms in subsurface layers in gray. Additionally, exemplarily Au-Au distances corresponding to certain peaks in the Patterson function, see Figure 8.2, are highlighted by connecting lines. Here, green, blue, pink, light green and magenta correspond to A, B, C, D and F respectively.

Using only in-plane diffraction data (or data with minimal out-of-plane momentum L) of reflections exclusive to the superstructure to generate the Patterson function P

$$P(U,V) = \sum_{j}^{N} |F(H_j, K_j, L \sim 0)|^2 \, e^{-2\pi i(H_j U + K_j V)} \ , \tag{8.5}$$

a projection of the inter-atomic distances in the unit cell of the superstructure onto the xy-plane is achieved granting (only) the lateral atomic distances making it easier to interpret the pattern of the Patterson function.
Figure 8.2(a) shows the experimental Patterson function for the (experimentally) recorded reflections. Since the Patterson function exhibits the same periodicity as the diffraction pattern used to compute it and only integer spots in the $\times$ 2 direction can be measured (see above for explanation) it exhibits a 5 $\times$ 1 periodicity. The $\times$ 2 periodicity of the unit cell is not lost, however, but instead it is back-folded into the $\times$ 1 periodicity of the Patterson function. A total of six distinct maxima (*A*-*F*) can be observed. *A*-*C* can be attributed to Au-Au-distances due to their high intensities. For *D*-*F* the assignment is not that straight forward however, and they could either be attributed to Au-Au- or Au-Si-distances. The Patterson functions $P(U,V)$ for the proposed structure models (coordinates for the AN-, EBH- and KK-model were supplied by Seino et al., see reference [61] for the AN- and the EBH-model coordinates and table A.1 in appendix A for the KK-model coordinates) were derived by first calculating the diffraction pattern for the particular model $|F_{model}(H_k, K_k, L_k)|^2$ and then applying equation 8.5 to only those reflections which were also recorded experimentally. The calculated Patterson functions $P(U,V)$ of all computed models exhibit the same six maxima, see Figure 8.2(b)-(d), however, the intensity of these maxima deviate quite strongly especially for the AN-model. Here, the maxima *A*, *C* and *F* display intensities significantly stronger then the intensity observed in the experimental Patterson function indicating that certain structural motifs of the AN-model do not comply with the "real" atomic structure of the 5 $\times$ 2 reconstruction. The intensity of the maxima of the EBH- and KK-model agree well with the experimental Patterson function for the maxima *A*, *B*, *C*, *E* and *F*, however, minor differences for the maximum *D* can be observed. Its intensity, which can be attributed to a Si-Au distance in the EBH- and a Au-Au distance in the KK-model (caused by the additional Au atom), in the experimental Patterson function lies between the intensities of the EBH- and the KK-model. Consequently, it is impossible to prefer one model over the other from this qualitative analysis.
The qualitative results are supported by the computation of the (crystallographic) R-factor [64]

$$R = \frac{\sum_k^N \, ||F_{exp}(H_k, K_k, L_k)| - |F_{model}(H_k, K_k, L_k)||}{\sum_j^N \, |F_{exp}(H_j, K_j, L_j)|} \tag{8.6}$$

for the in-plane data showing that the agreement between the AN-model and the experimental data is the worst with $R_{AN} = 0.3409$ as compared to the agreement of the EBH-model

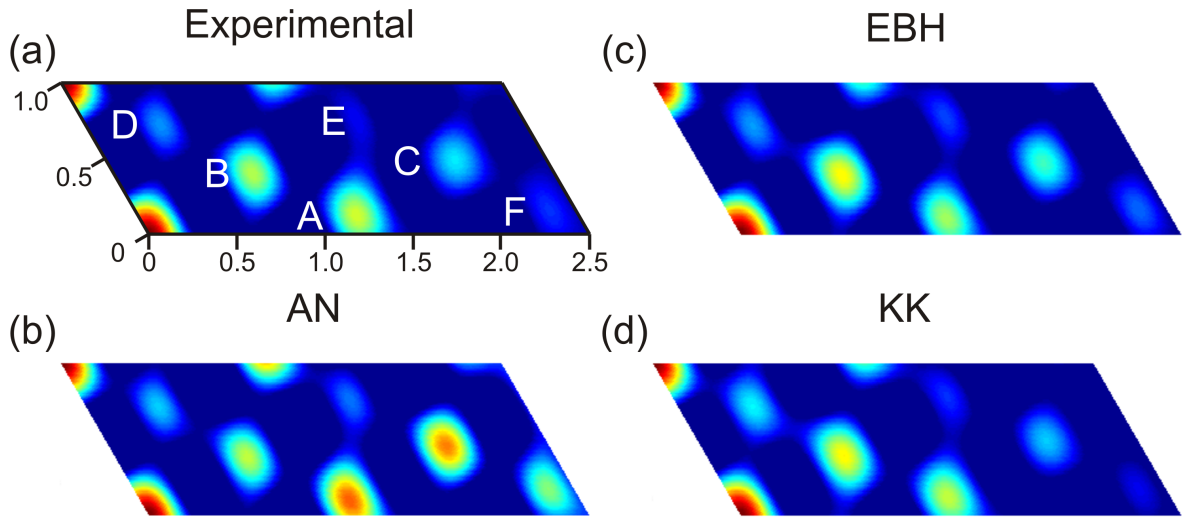

Figure 8.2: Experimental Patterson function and computed Patterson functions (in-plane) for the AN-, EBH- and the KK-model. The respective Patterson functions are only shown for the asymmetric unit of the observed 5 × 1 periodicity. A total of six different distinct maxima (labeled *A*-*F*) can be observed. The axes are scaled in the crystallographic coordinates used throughout the manuscript (1.0 corresponds to 3.84 Å).

$R_{EBH} = 0.1631$ and the KK-model $R_{KK} = 0.1475$ which exhibit lower R-factors. Consequently, the AN-model can be ruled out. This agrees with theoretical calculations [60, 61] and the SXRD results by Shirasawa et al [59]. The KK-model exhibits the lowest R-factor, however, the discrepancy between the EBH- and the KK-model is small, consequently the KK-model cannot be preferred over the EBH-model by comparison of the in-plane diffraction data with certainty and the experimental out-of-plane diffraction data (lattice rods) needs to be compared to the computed out-of-plane diffraction data as well.

8.3.2 Out-of-plane/Structural refinement

Figure 8.3 shows the intensity of the eight symmetry-inequivalent lattice rods (exclusive to the superstructure) recorded for the 5 × 2 reconstruction (blue). Calculating the χ^2-function (cf. chapter 2.4.3 equation 2.50)

$$\chi^2 = \frac{1}{N}\sum_{k=1}^{N}\frac{(|F_{k,exp}|^2 - |F_{k,model}|^2)^2}{\sigma^2_{k,exp}} \tag{8.7}$$

for the out-of-plane experimental data for the initial EBH- and KK-model (cf. Figure 8.1) shows that the KK-model agrees significantly better with the experimental data than the EBH model (χ^2(EBH) = 1.66 and χ^2(KK) = 1.21), giving a strong indication that the KK-model can be preferred over the EBH-model.

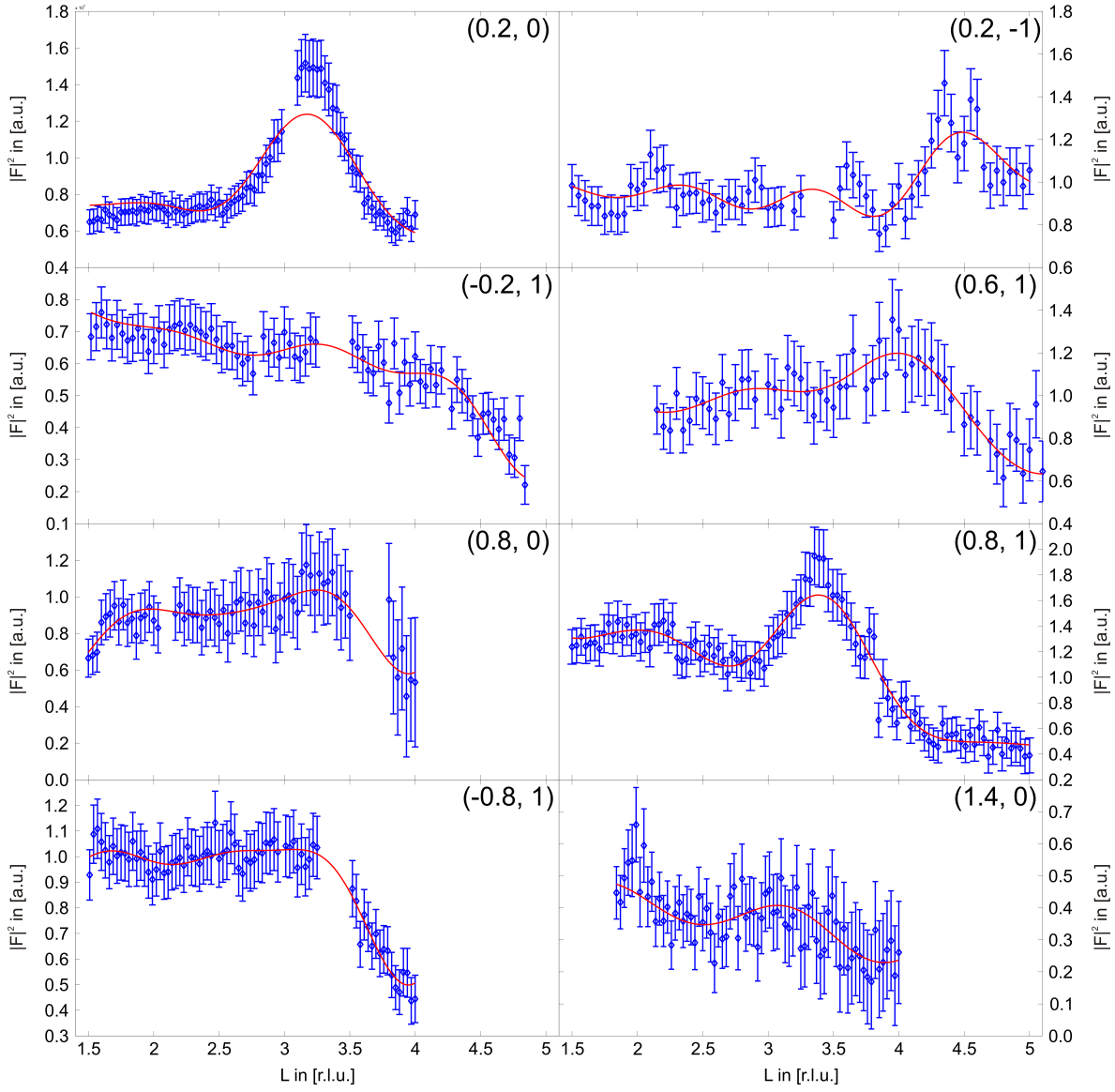

Figure 8.3: Display of the intensity of the eight symmetry-inequivalent lattice rods recorded for the 5 × 2 reconstruction (blue) and the corresponding (calculated) intensity of the refined KK-model (red) showing a very nice agreement.

During refinement groups of atoms (composed of one or more atoms) were allowed to move from their initial positions. The starting models (EBH, KK), cf. Figure 8.1, contain three subsurface Si double-layers and the (topmost) layer containing the Au atoms. Due to the low symmetry of the unit cell (P_1 symmetry), in principal, no constraints are imposed upon the movement of the individual atoms in respect to the movement of other atoms in the refinement process as no symmetry elements exist (apart from the identity). However, due to the fact that the structure of the 5×2 unit cell is very similar for both 5×1 sub-units (apart from the dimerization of two Au atoms (EBH, KK) and the additional Au atom in one of the sub units (KK)) it is defensible to assume the same deviation from the initial position for "equal" atoms in both sub-units (at least for the subsurface Si double-layers) reducing the number of parameters for the subsurface Si atoms to half the number required otherwise. For the topmost layer the Au atoms are allowed to move independently of one another as are the Si atoms that are not part of the honeycomb-like ring. The Si atoms in the honeycomb, however, were coupled in such a way that their lateral positions do not change with respect to one another and were only allowed to move vertically independently because the honeycomb structure is integral to explaining e.g. reflectance anisotropy spectroscopic features of the reconstruction [60].
The structure was refined by allowing deviations (from the initial positions) in all crystallographic directions even though the out-of-plane data should be more sensitive to vertical deviations because the agreement between calculated and experimental intensity could be improved significantly this way. In order to suppress physically unrealistic bonding-angles and -lengths during fitting we employed a Keating model approach [24] and defined the following goodness of fit (gof) [25, 65]

$$gof = \chi^2 + kE_{Keat} \quad , \tag{8.8}$$

where E_{Keat} is the Keating-energy and k is its weighting factor. During optimization the weighting factor k was decreased gradually eventually only least-square fitting the calculated to the experimental recorded intensities. Refining the EBH-model grants a χ^2-value of

$$\chi^2(\mathrm{EBH_{refined}}) \;\geq\; 2\chi^2(\mathrm{KK_{refined}}) \;, \tag{8.9}$$

which further manifests that the KK-model should/can be preferred over the EBH-model. Figure 8.3 shows a very nice agreement between the intensity of the eight lattice rods recorded for the 5×2 reconstruction (blue) and the corresponding (calculated) intensity of the model obtained by the refinement of the KK-model (red) with a χ^2-value of $\chi^2(\mathrm{KK_{refined}}) = 0.42$. The atomic positions for the KK-model granted by the refinement procedure are given in table A.2 in appendix A.

The undulation of the intensity observed for some of the lattice rods (especially for [$H = 0.2$, $K = 0$] and [$H = 0.8$, $K = 1.0$]) already indicates that the surface might be more corrugated than assumed in the starting (KK-)model. Indeed, analyzing the deviations from the starting (KK-)model, see Figure 8.4, one finds that all Au atoms experience an elevation except one (dashed blue circle) whereas the Si atoms in the topmost layer experience a depression except one (dashed blue circle). Additionally, this depression of Si atoms is non-uniform leading to

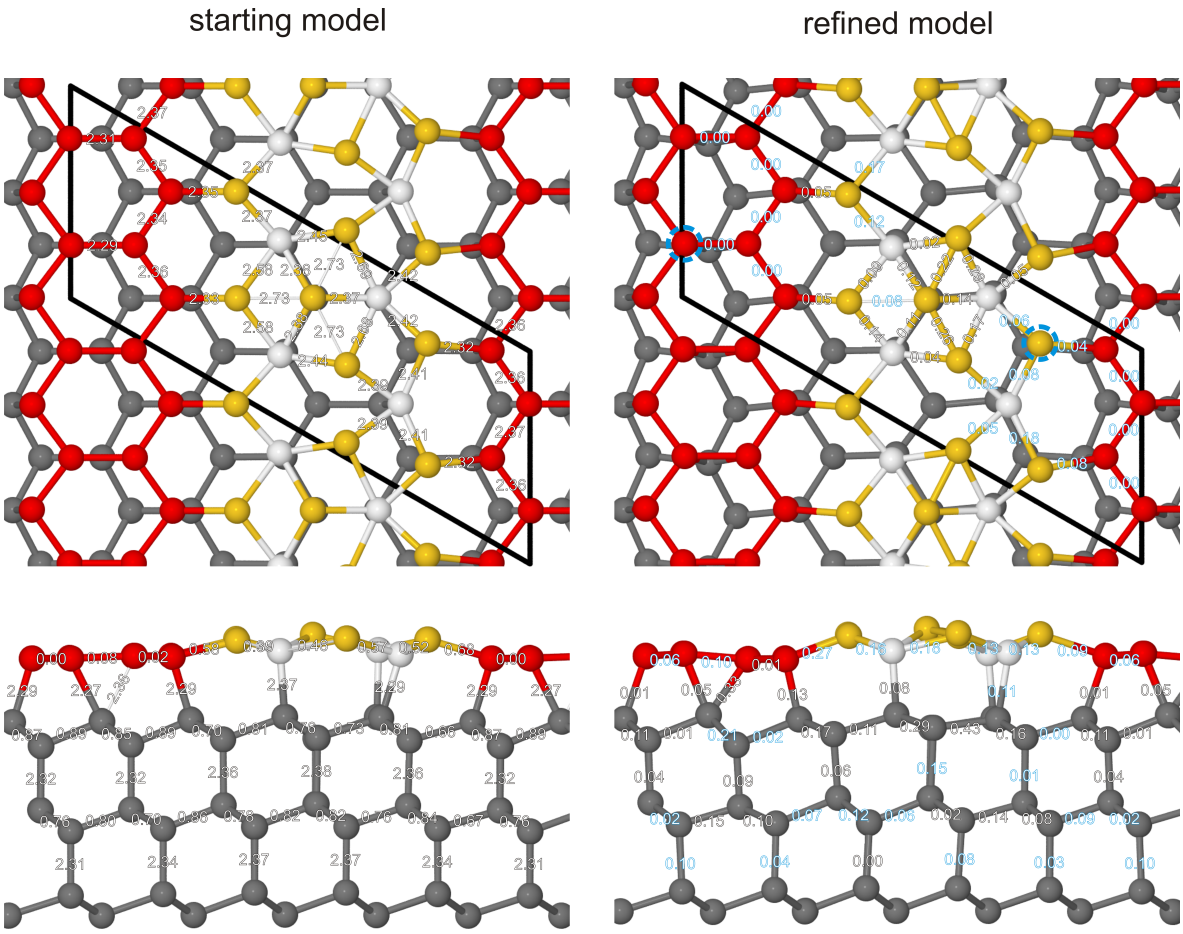

Figure 8.4: Display of the starting (KK-)model (left) and the refined (KK-)model (right). The projected distances (given in Å) between adjacent atoms are shown for the starting model (black numbers on the lefthand side). For the refined model the difference in magnitude of the (projected) distance $\Delta r = r_{ref}$ - r_{start} between the refined and the starting model is displayed. Here, blue numbers correspond to an increase and black numbers to a decrease in distance. For the top view (top) the distances are projected into the xy-plane whereas they are projected onto the z-axis for the side view (bottom). The Au atom which experiences a depression and the Si atom which experiences an elevation during the refinement (cf. text) are highlighted by dashed blue circles.

a vertical tilting of the honeycomb structure. The topmost layer is also changed horizontally with the most glaring difference being the movement of the surrounding atoms mostly towards the "additional" (as compared to the EBH-model) Au atom (five out of six atoms do so). The subsurface Si structure is changed as well which is most pronounced directly underneath the Au rows. This change in structure reaches down up to the third subsurface layer where the atomic distances still exhibit values different from the one expected for a perfect bulk structure (= 2.352 Å).

8.4 Conclusion

By the comparison of the Patterson function generated from experimentally collected in-plane diffraction data to the computed Patterson function for the EBH-, AN- and KK-model we were able to rule out the AN-model. Furthermore, we were able to show that the KK-model is more probable than the EBH-model by the comparison of experimentally collected out-of-plane data to their computed counter-part for the EBH- and KK-model and the subsequent refinement of these structure models. This further cements the KK-model as the state of the art model which is in concurrence with the results obtained by Shirasawa et al. [59]. However, contrary to the refined structure model proposed by Shirasawa et al., which only contains two subsurface Si layers our refined structure model reaches deeper into the crystal with three subsurface Si layers. The need for an additional subsurface Si layer can be attributed to the fact that the lattice rods we recorded exhibit strong undulations which are not observed for the lattice rods and crystal truncation rods recorded by Shirasawa et al. Consequently, their refined structure model is mostly insensitive to the changes in the subsurface Si layers causing these undulations whereas our refined structure model contains this information.

9 Summary and Outlook

In this thesis the morphology and the atomic structure of quasi-one-dimensional structures grown on Si were determined by means of diffraction experiments in combination with kinematic diffraction theory calculations.
In the first and the second study the formerly unknown $\left(2\sqrt{3} \times \sqrt{3}\right)$ R30° reconstruction on Si(111) was characterized by means of STM, DFT, SPA-LEED experiments and kinematic diffraction calculations. Here, a structure model could be proposed which contains half as many subsurface Si vacancies as compared to the well-known $\left(\sqrt{3} \times \sqrt{3}\right)$ R30° reconstruction on Si(111) it was derived from. Due to the decreased number of subsurface Si vacancies the reconstruction is subject to an uni-axial strain which is mitigated by the formation of domains separated by anti-phase domain boundaries. It could be shown that two different types of domains alternate across the surface forming quasi-one-dimensional domains. Additionally, the distribution of the domains could be derived by comparison with kinematic diffraction calculations. In this thesis only structural features of this quasi-one-dimensional structure were investigated, additional studies probing the electronic structure could be performed. Here, e.g., Angle-resolved Photoelectron Spectroscopy and/or Density Functional Theory calculations could be performed in order to show whether the electronic structure is one-dimensional as well. Additionally, SXRD experiments could be performed in order to assess the validity of the structure model proposed.
In the third study a deeper insight into the complex system of bundled rare-earth silicide nanowires on Si(001) was given. Here, the distributions of the NW width, the bundle width and the bundle distance were deduced from the diffraction patterns collected by SPA-LEED and the subsequent comparison to kinematic diffraction theory calculations. Additionally, it was shown that the (2×1) reconstruction sometimes observed on top of the NWs by STM cannot exist over larger parts of the sample and instead a (1×1) reconstruction needs to be assumed to explain the experimentally observed diffraction data. Here, varying the heating procedure during preparation (e.g., post deposition annealing vs quenching after evaporation) and additional experiments evaporating different rare-earth silicides could help to determine whether the underlying NW distributions are strongly influenced by it. Additionally, the influence of the substrate could be investigated more thoroughly by e.g., changing the angle of inclination in respect to the Si(001) surface (vicinal surfaces). Here, it would be interesting to determine whether the decrease of the mean terrace size (accompanying the increase in the angle of inclination) influences the distribution of the NW width or not and if the growth of the (bundled) NWs causes a major structural change in the terrace structure (e.g., refacetting of the surface).
In the fourth study the atomic structure of the gold induced atomic wires of the Si(111)-(5×2)-Au system was analyzed. The Patterson function of the in-plane SXRD data was compared to the Patterson functions derived from the atomic structure models proposed in literature (AN, EBH, KK) ruling out the AN-model. By comparison of the experimental out-of-plane SXRD data to the corresponding (calculated) SXRD data for the EBH- and the KK-model the KK-model could be identified as the most probable model. Additionally, a refined atomic structure model was derived for the KK-model. Here, complementary diffraction methods (e.g., quantitative LEED, Transmission Electron Microscopy) in addition to Density Func-

tional Theory calculations could be employed in order assess and/or further refine the atomic structure model.
In conclusion, the results presented in this thesis clearly display the power of diffraction experiments especially in conjunction with the comparison to kinematic diffraction theory calculations and prove that they are applicable even to low dimensional (e.g., quasi-one-dimensional) structures. Furthermore, it was shown that diffraction experiments can deliver complementary information (e.g., information on deeper atomic layers) as compared to local probing methods (e.g. STM or Atomic Force Microscopy) and especially the combination of local probing methods, DFT calculations and diffraction experiments allows for the explanation of even very complicated material systems.

A Coordinates of the Si(111)-(5×2)-Au-Reconstruction (KK-model)

Nr.	Element	Position [surface units]	(u_{11}, u_{12}, u_{13}, u_{22}, u_{23}, u_{33}) [Å^2]
1	Au	(0.5275, 0.6614, 1.0808)	(0.0000, 0.0000, 0.0000, 0.0000, 0.0000, 0.0000)
2	Au	(0.7777, 0.7597, 1.0612)	(0.0000, 0.0000, 0.0000, 0.0000, 0.0000, 0.0000)
3	Au	(0.7781, 0.1869, 1.0611)	(0.0000, 0.0000, 0.0000, 0.0000, 0.0000, 0.0000)
4	Au	(0.6021, 0.4371, 1.0658)	(0.0000, 0.0000, 0.0000, 0.0000, 0.0000, 0.0000)
5	Au	(0.6013, 0.0715, 1.0660)	(0.0000, 0.0000, 0.0000, 0.0000, 0.0000, 0.0000)
6	Au	(0.3609, 0.9538, 1.0630)	(0.0000, 0.0000, 0.0000, 0.0000, 0.0000, 0.0000)
7	Au	(0.3632, 0.4541, 1.0585)	(0.0000, 0.0000, 0.0000, 0.0000, 0.0000, 0.0000)
8	Si	(0.1376, 0.9235, 0.9982)	(0.0000, 0.0000, 0.0000, 0.0000, 0.0000, 0.0000)
9	Si	(0.1400, 0.4244, 0.9985)	(0.0000, 0.0000, 0.0000, 0.0000, 0.0000, 0.0000)
10	Si	(0.9166, 0.8989, 0.9886)	(0.0000, 0.0000, 0.0000, 0.0000, 0.0000, 0.0000
11	Si	(0.9173, 0.3939, 0.9887)	(0.0000, 0.0000, 0.0000, 0.0000, 0.0000, 0.0000
12	Si	(0.6703, 0.8395, 1.0205)	(0.0000, 0.0000, 0.0000, 0.0000, 0.0000, 0.0000
13	Si	(0.7182, 0.3986, 1.0050)	(0.0000, 0.0000, 0.0000, 0.0000, 0.0000, 0.0000
14	Si	(0.4555, 0.8405, 1.0166)	(0.0000, 0.0000, 0.0000, 0.0000, 0.0000, 0.0000
15	Si	(0.4567, 0.3023, 1.0166)	(0.0000, 0.0000, 0.0000, 0.0000, 0.0000, 0.0000
16	Si	(0.2194, 0.7759, 0.9983)	(0.0000, 0.0000, 0.0000, 0.0000, 0.0000, 0.0000
17	Si	(0.2227, 0.2777, 0.9961)	(0.0000, 0.0000, 0.0000, 0.0000, 0.0000, 0.0000
18	Si	(-0.0014, 0.7493, 0.9918)	(0.0000, 0.0000, 0.0000, 0.0000, 0.0000, 0.0000)
19	Si	(0.0018, 0.2516, 0.9893)	(0.0000, 0.0000, 0.0000, 0.0000, 0.0000, 0.0000)
20	Si	(0.8750, 0.8459, 0.7447)	(0.0000, 0.0000, 0.0000, 0.0000, 0.0000, 0.0000)
21	Si	(0.8755, 0.3424, 0.7447)	(0.0000, 0.0000, 0.0000, 0.0000, 0.0000, 0.0000)
22	Si	(0.6679, 0.8358, 0.7652)	(0.0000, 0.0000, 0.0000, 0.0000, 0.0000, 0.0000)
23	Si	(0.6770, 0.3467, 0.7607)	(0.0000, 0.0000, 0.0000, 0.0000, 0.0000, 0.0000)
24	Si	(0.4663, 0.8376, 0.7646)	(0.0000, 0.0000, 0.0000, 0.0000, 0.0000, 0.0000)
25	Si	(0.4669, 0.3308, 0.7645)	(0.0000, 0.0000, 0.0000, 0.0000, 0.0000, 0.0000)
26	Si	(0.2610, 0.8272, 0.7546)	(0.0000, 0.0000, 0.0000, 0.0000, 0.0000, 0.0000)
27	Si	(0.2625, 0.3278, 0.7520)	(0.0000, 0.0000, 0.0000, 0.0000, 0.0000, 0.0000)
28	Si	(0.0679, 0.8357, 0.7488)	(0.0000, 0.0000, 0.0000, 0.0000, 0.0000, 0.0000)
29	Si	(0.0695, 0.3368, 0.7475)	(0.0000, 0.0000, 0.0000, 0.0000, 0.0000, 0.0000)
30	Si	(0.9353, 0.6695, 0.6533)	(0.0000, 0.0000, 0.0000, 0.0000, 0.0000, 0.0000)
31	Si	(0.9373, 0.1713, 0.6520)	(0.0000, 0.0000, 0.0000, 0.0000, 0.0000, 0.0000)
32	Si	(0.7380, 0.6780, 0.6743)	(0.0000, 0.0000, 0.0000, 0.0000, 0.0000, 0.0000)
33	Si	(0.7383, 0.1685, 0.6743)	(0.0000, 0.0000, 0.0000, 0.0000, 0.0000, 0.0000)
34	Si	(0.5333, 0.6677, 0.6820)	(0.0000, 0.0000, 0.0000, 0.0000, 0.0000, 0.0000)
35	Si	(0.5388, 0.1740, 0.6830)	(0.0000, 0.0000, 0.0000, 0.0000, 0.0000, 0.0000)
36	Si	(0.3322, 0.6673, 0.6776)	(0.0000, 0.0000, 0.0000, 0.0000, 0.0000, 0.0000)
37	Si	(0.3328, 0.1645, 0.6776)	(0.0000, 0.0000, 0.0000, 0.0000, 0.0000, 0.0000)
38	Si	(0.1319, 0.6662, 0.6575)	(0.0000, 0.0000, 0.0000, 0.0000, 0.0000, 0.0000)
39	Si	(0.1327, 0.1654, 0.6569)	(0.0000, 0.0000, 0.0000, 0.0000, 0.0000, 0.0000)
40	Si	(0.9348, 0.6690, 0.4064)	(0.0000, 0.0000, 0.0000, 0.0000, 0.0000, 0.0000)
41	Si	(0.9353, 0.1694, 0.4053)	(0.0000, 0.0000, 0.0000, 0.0000, 0.0000, 0.0000)
42	Si	(0.7349, 0.6716, 0.4231)	(0.0000, 0.0000, 0.0000, 0.0000, 0.0000, 0.0000)
43	Si	(0.7349, 0.1670, 0.4232)	(0.0000, 0.0000, 0.0000, 0.0000, 0.0000, 0.0000)
44	Si	(0.5333, 0.6672, 0.4291)	(0.0000, 0.0000, 0.0000, 0.0000, 0.0000, 0.0000)
45	Si	(0.5356, 0.1698, 0.4299)	(0.0000, 0.0000, 0.0000, 0.0000, 0.0000, 0.0000)
46	Si	(0.3336, 0.6676, 0.4259)	(0.0000, 0.0000, 0.0000, 0.0000, 0.0000, 0.0000)
47	Si	(0.3338, 0.1666, 0.4259)	(0.0000, 0.0000, 0.0000, 0.0000, 0.0000, 0.0000)
48	Si	(0.1323, 0.6660, 0.4098)	(0.0000, 0.0000, 0.0000, 0.0000, 0.0000, 0.0000)
49	Si	(0.1326, 0.1656, 0.4093)	(0.0000, 0.0000, 0.0000, 0.0000, 0.0000, 0.0000)
50	Si	(0.7991, 0.4997, 0.3367)	(0.0000, 0.0000, 0.0000, 0.0000, 0.0000, 0.0000)

Nr.	Element	Position [surface units]	(u_{11}, u_{12}, u_{13}, u_{22}, u_{23}, u_{33}) [Å^2]
51	Si	(0.8002, 0.0009, 0.3333)	(0.0000, 0.0000, 0.0000, 0.0000, 0.0000, 0.0000)
52	Si	(0.6005, 0.5019, 0.3423)	(0.0000, 0.0000, 0.0000, 0.0000, 0.0000, 0.0000)
53	Si	(0.6006, 0.0004, 0.3423)	(0.0000, 0.0000, 0.0000, 0.0000, 0.0000, 0.0000)
54	Si	(0.4004, 0.5006, 0.3417)	(0.0000, 0.0000, 0.0000, 0.0000, 0.0000, 0.0000)
55	Si	(0.4018, 0.0021, 0.3427)	(0.0000, 0.0000, 0.0000, 0.0000, 0.0000, 0.0000)
56	Si	(0.2016, 0.5024, 0.3343)	(0.0000, 0.0000, 0.0000, 0.0000, 0.0000, 0.0000)
57	Si	(0.2018, 0.0021, 0.3341)	(0.0000, 0.0000, 0.0000, 0.0000, 0.0000, 0.0000)
58	Si	(0.0005, 0.5014, 0.3244)	(0.0000, 0.0000, 0.0000, 0.0000, 0.0000, 0.0000)
59	Si	(0.0007, 0.0009, 0.3242)	(0.0000, 0.0000, 0.0000, 0.0000, 0.0000, 0.0000)
60	Si	(0.7995, 0.5004, 0.0861)	(0.0000, 0.0000, 0.0000, 0.0000, 0.0000, 0.0000)
61	Si	(0.7998, 0.0008, 0.0839)	(0.0000, 0.0000, 0.0000, 0.0000, 0.0000, 0.0000)
62	Si	(0.6002, 0.5012, 0.0902)	(0.0000, 0.0000, 0.0000, 0.0000, 0.0000, 0.0000)
63	Si	(0.6002, 0.0007, 0.0902)	(0.0000, 0.0000, 0.0000, 0.0000, 0.0000, 0.0000)
64	Si	(0.4008, 0.5013, 0.0898)	(0.0000, 0.0000, 0.0000, 0.0000, 0.0000, 0.0000)
65	Si	(0.4013, 0.0019, 0.0903)	(0.0000, 0.0000, 0.0000, 0.0000, 0.0000, 0.0000)
66	Si	(0.2015, 0.5020, 0.0846)	(0.0000, 0.0000, 0.0000, 0.0000, 0.0000, 0.0000)
67	Si	(0.2017, 0.0019, 0.0845)	(0.0000, 0.0000, 0.0000, 0.0000, 0.0000, 0.0000)
68	Si	(0.0005, 0.5012, 0.0777)	(0.0000, 0.0000, 0.0000, 0.0000, 0.0000, 0.0000)
69	Si	(0.0006, 0.0008, 0.0776)	(0.0000, 0.0000, 0.0000, 0.0000, 0.0000, 0.0000)
70	Si	(0.8663, 0.8333, 0.0011)	(0.0000, 0.0000, 0.0000, 0.0000, 0.0000, 0.0000)
71	Si	(0.8663, 0.3343, 0.0012)	(0.0000, 0.0000, 0.0000, 0.0000, 0.0000, 0.0000)
72	Si	(0.6662, 0.8335, 0.0032)	(0.0000, 0.0000, 0.0000, 0.0000, 0.0000, 0.0000)
73	Si	(0.6661, 0.3334, 0.0036)	(0.0000, 0.0000, 0.0000, 0.0000, 0.0000, 0.0000)
74	Si	(0.4672, 0.8342, 0.0041)	(0.0000, 0.0000, 0.0000, 0.0000, 0.0000, 0.0000)
75	Si	(0.4672, 0.3344, 0.0041)	(0.0000, 0.0000, 0.0000, 0.0000, 0.0000, 0.0000)
76	Si	(0.2684, 0.8354, 0.0025)	(0.0000, 0.0000, 0.0000, 0.0000, 0.0000, 0.0000)
77	Si	(0.2681, 0.3352, 0.0022)	(0.0000, 0.0000, 0.0000, 0.0000, 0.0000, 0.0000)
78	Si	(0.0684, 0.8356, 0.0000)	(0.0000, 0.0000, 0.0000, 0.0000, 0.0000, 0.0000)
79	Si	(0.0682, 0.3356, 0.0001)	(0.0000, 0.0000, 0.0000, 0.0000, 0.0000, 0.0000)

Table A.1: Structure of the Si(111)-(5×2)-Au-Reconstruction (KK-model) (cf. chapter 8). The positions of the atoms are given in surface units and the atomic displacement factors in Å^2.

Nr.	Element	Position [surface units]	(u_{11}, u_{12}, u_{13}, u_{22}, u_{23}, u_{33}) [Å^2]
1	Au	(0.5334, 0.6505, 1.0854)	(0.0087, 0.0072, 0.0000, 0.0063, 0.0000, 0.0000)
2	Au	(0.7793, 0.7531, 1.0664)	(0.0087, 0.0072, 0.0000, 0.0063, 0.0000, 0.0000)
3	Au	(0.7797, 0.1595, 1.0652)	(0.0087, 0.0072, 0.0000, 0.0063, 0.0000, 0.0000)
4	Au	(0.6028, 0.4520, 1.0590)	(0.0087, 0.0072, 0.0000, 0.0063, 0.0000, 0.0000)
5	Au	(0.6020, 0.0273, 1.0697)	(0.0087, 0.0072, 0.0000, 0.0063, 0.0000, 0.0000)
6	Au	(0.3615, 0.9309, 1.0641)	(0.0087, 0.0072, 0.0000, 0.0063, 0.0000, 0.0000)
7	Au	(0.3638, 0.4311, 1.0601)	(0.0087, 0.0072, 0.0000, 0.0063, 0.0000, 0.0000)
8	Si	(0.1421, 0.9287, 0.9700)	(0.0000, 0.0139, 0.0000, 0.0017, 0.0000, 0.0000)
9	Si	(0.1446, 0.4296, 0.9700)	(0.0000, 0.0139, 0.0000, 0.0017, 0.0000, 0.0000)
10	Si	(0.9211, 0.9041, 0.9810)	(0.0000, 0.0139, 0.0000, 0.0017, 0.0000, 0.0000)
11	Si	(0.9218, 0.3990, 0.9831)	(0.0000, 0.0139, 0.0000, 0.0017, 0.0000, 0.0000)
12	Si	(0.6671, 0.8287, 0.9935)	(0.0000, 0.0139, 0.0000, 0.0017, 0.0000, 0.0000)
13	Si	(0.7109, 0.3778, 0.9947)	(0.0000, 0.0139, 0.0000, 0.0017, 0.0000, 0.0000)
14	Si	(0.4576, 0.8010, 1.0013)	(0.0000, 0.0139, 0.0000, 0.0017, 0.0000, 0.0000)
15	Si	(0.4591, 0.3089, 1.0003)	(0.0000, 0.0139, 0.0000, 0.0017, 0.0000, 0.0000)
16	Si	(0.2240, 0.7810, 0.9727)	(0.0000, 0.0139, 0.0000, 0.0017, 0.0000, 0.0000)
17	Si	(0.2272, 0.2828, 0.9686)	(0.0000, 0.0139, 0.0000, 0.0017, 0.0000, 0.0000)
18	Si	(0.0031, 0.7544, 0.9917)	(0.0000, 0.0139, 0.0000, 0.0017, 0.0000, 0.0000)
19	Si	(0.0063, 0.2567, 0.9904)	(0.0000, 0.0139, 0.0000, 0.0017, 0.0000, 0.0000)
20	Si	(0.8749, 0.8370, 0.7403)	(0.0000, 0.0000, 0.0000, 0.0000, 0.0072, 0.0000)
21	Si	(0.8753, 0.3335, 0.7404)	(0.0000, 0.0000, 0.0000, 0.0000, 0.0072, 0.0000)
22	Si	(0.6776, 0.8606, 0.7427)	(0.0000, 0.0000, 0.0000, 0.0000, 0.0072, 0.0000)
23	Si	(0.6868, 0.3715, 0.7382)	(0.0000, 0.0000, 0.0000, 0.0000, 0.0072, 0.0000)
24	Si	(0.4665, 0.8404, 0.7572)	(0.0000, 0.0000, 0.0000, 0.0000, 0.0072, 0.0000)
25	Si	(0.4670, 0.3336, 0.7571)	(0.0000, 0.0000, 0.0000, 0.0000, 0.0072, 0.0000)
26	Si	(0.2540, 0.8158, 0.7414)	(0.0000, 0.0000, 0.0000, 0.0000, 0.0072, 0.0000)
27	Si	(0.2555, 0.3165, 0.7388)	(0.0000, 0.0000, 0.0000, 0.0000, 0.0072, 0.0000)
28	Si	(0.0577, 0.7913, 0.7555)	(0.0000, 0.0000, 0.0000, 0.0000, 0.0072, 0.0000)
29	Si	(0.0592, 0.2924, 0.7542)	(0.0000, 0.0000, 0.0000, 0.0000, 0.0072, 0.0000)
30	Si	(0.9255, 0.6593, 0.6616)	(0.0000, 0.0000, 0.0000, 0.0000, 0.0072, 0.0000)
31	Si	(0.9275, 0.1611, 0.6604)	(0.0000, 0.0000, 0.0000, 0.0000, 0.0072, 0.0000)
32	Si	(0.7470, 0.6969, 0.6695)	(0.0000, 0.0000, 0.0000, 0.0000, 0.0072, 0.0000)
33	Si	(0.7474, 0.1874, 0.6695)	(0.0000, 0.0000, 0.0000, 0.0000, 0.0072, 0.0000)
34	Si	(0.5420, 0.6654, 0.7056)	(0.0000, 0.0000, 0.0000, 0.0000, 0.0072, 0.0000)
35	Si	(0.5475, 0.1718, 0.7067)	(0.0000, 0.0000, 0.0000, 0.0000, 0.0072, 0.0000)
36	Si	(0.3296, 0.6601, 0.6829)	(0.0000, 0.0000, 0.0000, 0.0000, 0.0072, 0.0000)
37	Si	(0.3302, 0.1573, 0.6829)	(0.0000, 0.0000, 0.0000, 0.0000, 0.0072, 0.0000)
38	Si	(0.1183, 0.6170, 0.6411)	(0.0000, 0.0000, 0.0000, 0.0000, 0.0072, 0.0000)
39	Si	(0.1191, 0.1162, 0.6405)	(0.0000, 0.0000, 0.0000, 0.0000, 0.0072, 0.0000)
40	Si	(0.9319, 0.6707, 0.4200)	(0.0000, 0.0000, 0.0000, 0.0000, 0.0072, 0.0000)
41	Si	(0.9324, 0.1712, 0.4189)	(0.0000, 0.0000, 0.0000, 0.0000, 0.0072, 0.0000)
42	Si	(0.7457, 0.7077, 0.4171)	(0.0000, 0.0000, 0.0000, 0.0000, 0.0072, 0.0000)
43	Si	(0.7458, 0.2031, 0.4171)	(0.0000, 0.0000, 0.0000, 0.0000, 0.0072, 0.0000)
44	Si	(0.5390, 0.6877, 0.4359)	(0.0000, 0.0000, 0.0000, 0.0000, 0.0072, 0.0000)
45	Si	(0.5412, 0.1904, 0.4367)	(0.0000, 0.0000, 0.0000, 0.0000, 0.0072, 0.0000)
46	Si	(0.3396, 0.6994, 0.4384)	(0.0000, 0.0000, 0.0000, 0.0000, 0.0072, 0.0000)
47	Si	(0.3398, 0.1983, 0.4384)	(0.0000, 0.0000, 0.0000, 0.0000, 0.0072, 0.0000)
48	Si	(0.1262, 0.6628, 0.4035)	(0.0000, 0.0000, 0.0000, 0.0000, 0.0072, 0.0000)
49	Si	(0.1264, 0.1623, 0.4031)	(0.0000, 0.0000, 0.0000, 0.0000, 0.0072, 0.0000)
50	Si	(0.8007, 0.5111, 0.3400)	(0.0000, 0.0000, 0.0000, 0.0000, 0.0072, 0.0000)

Nr.	Element	Position [surface units]	(u_{11}, u_{12}, u_{13}, u_{22}, u_{23}, u_{33}) [Å^2]
51	Si	(0.8017, 0.0123, 0.3366)	(0.0000, 0.0000, 0.0000, 0.0000, 0.0072, 0.0000)
52	Si	(0.6094, 0.5253, 0.3518)	(0.0000, 0.0000, 0.0000, 0.0000, 0.0072, 0.0000)
53	Si	(0.6095, 0.0238, 0.3517)	(0.0000, 0.0000, 0.0000, 0.0000, 0.0072, 0.0000)
54	Si	(0.4070, 0.5332, 0.3414)	(0.0000, 0.0000, 0.0000, 0.0000, 0.0072, 0.0000)
55	Si	(0.4084, 0.0348, 0.3424)	(0.0000, 0.0000, 0.0000, 0.0000, 0.0072, 0.0000)
56	Si	(0.2045, 0.5193, 0.3388)	(0.0000, 0.0000, 0.0000, 0.0000, 0.0072, 0.0000)
57	Si	(0.2048, 0.0190, 0.3386)	(0.0000, 0.0000, 0.0000, 0.0000, 0.0072, 0.0000)
58	Si	(0.9941, 0.5049, 0.3351)	(0.0000, 0.0000, 0.0000, 0.0000, 0.0072, 0.0000)
59	Si	(0.9943, 0.0044, 0.3349)	(0.0000, 0.0000, 0.0000, 0.0000, 0.0072, 0.0000)
60	Si	(0.7995, 0.5004, 0.0861)	(0.0000, 0.0000, 0.0000, 0.0000, 0.0072, 0.0000)
61	Si	(0.7999, 0.0008, 0.0839)	(0.0000, 0.0000, 0.0000, 0.0000, 0.0072, 0.0000)
62	Si	(0.6002, 0.5012, 0.0902)	(0.0000, 0.0000, 0.0000, 0.0000, 0.0072, 0.0000)
63	Si	(0.6002, 0.0007, 0.0902)	(0.0000, 0.0000, 0.0000, 0.0000, 0.0072, 0.0000)
64	Si	(0.4008, 0.5013, 0.0898)	(0.0000, 0.0000, 0.0000, 0.0000, 0.0072, 0.0000)
65	Si	(0.4013, 0.0019, 0.0903)	(0.0000, 0.0000, 0.0000, 0.0000, 0.0072, 0.0000)
66	Si	(0.2015, 0.5020, 0.0846)	(0.0000, 0.0000, 0.0000, 0.0000, 0.0072, 0.0000)
67	Si	(0.2017, 0.0019, 0.0845)	(0.0000, 0.0000, 0.0000, 0.0000, 0.0072, 0.0000)
68	Si	(0.0005, 0.5012, 0.0777)	(0.0000, 0.0000, 0.0000, 0.0000, 0.0072, 0.0000)
69	Si	(0.0006, 0.0008, 0.0776)	(0.0000, 0.0000, 0.0000, 0.0000, 0.0072, 0.0000)
70	Si	(0.8663, 0.8333, 0.0011)	(0.0000, 0.0000, 0.0000, 0.0000, 0.0072, 0.0000)
71	Si	(0.8663, 0.3343, 0.0012)	(0.0000, 0.0000, 0.0000, 0.0000, 0.0072, 0.0000)
72	Si	(0.6661, 0.8335, 0.0032)	(0.0000, 0.0000, 0.0000, 0.0000, 0.0072, 0.0000)
73	Si	(0.6661, 0.3334, 0.0036)	(0.0000, 0.0000, 0.0000, 0.0000, 0.0072, 0.0000)
74	Si	(0.4672, 0.8342, 0.0041)	(0.0000, 0.0000, 0.0000, 0.0000, 0.0072, 0.0000)
75	Si	(0.4672, 0.3344, 0.0041)	(0.0000, 0.0000, 0.0000, 0.0000, 0.0072, 0.0000)
76	Si	(0.2684, 0.8354, 0.0025)	(0.0000, 0.0000, 0.0000, 0.0000, 0.0072, 0.0000)
77	Si	(0.2681, 0.3352, 0.0022)	(0.0000, 0.0000, 0.0000, 0.0000, 0.0072, 0.0000)
78	Si	(0.0684, 0.8356, 0.0000)	(0.0000, 0.0000, 0.0000, 0.0000, 0.0072, 0.0000)
79	Si	(0.0682, 0.3356, 0.0001)	(0.0000, 0.0000, 0.0000, 0.0000, 0.0072, 0.0000)

Table A.2: Structure of the Si(111)-(5×2)-Au-Reconstruction after refinement (KK-model) (cf. chapter 8). The positions of the atoms are given in surface units and the atomic displacement factors in Å^2.

B List of peer-reviewed publications

- F. Bertram, C. Deiter, O. Hoefert, T. Schemme, F. Timmer, M. Suendorf, B. Zimmermann, J. Wollschläger
  X-ray diffraction study on size effects in epitaxial magnetite thin films on MgO(001)
  Journal of Physics D **45**, 395302 (2012).
  available at `https://doi.org/10.1088/0022-3727/45/39/395302`

- S. Sanna, C. Dues, W. G. Schmidt, F. Timmer, J. Wollschläger, M. Franz, S. Appelfeller, M. Dähne
  Rare-earth silicide thin films on the Si(111) surface
  Physical Review B **93**, 195407 (2016).
  available at `https://doi.org/10.1103/PhysRevB.93.195407`

- F. Timmer, R. Oelke, C. Dues, S. Sanna, W. G. Schmidt, M. Franz, S. Appelfeller, M. Dähne, J. Wollschläger
  Strain-induced quasi-one-dimensional rare-earth silicides structures on Si(111)
  Physical Review B **94**, 205431 (2016).
  available at `https://doi.org/10.1103/PhysRevB.94.205431`

- F. Timmer, J. Wollschläger
  Effects of Domain Boundaries on the Diffraction Patterns of One-Dimensional Structures
  Condensed Matter **2**, 7 (2017).
  available at `https://doi.org/10.3390/condmat2010007`

- F. Timmer, J. Bahlmann, J. Wollschläger
  On the diffraction pattern of bundled rare-earth silicide Nanowires on Si(001)
  Journal of Physics: Condensed Matter **29**, 435304 (2017).
  available at `https://doi.org/10.1088/1361-648X/aa8845`

References

[1] R. E. Peierls. *Quantum Theory of Solids*. Clarendon Press, 1964.

[2] F. D. M. Haldane. 'Luttinger liquid theory' of one-dimensional quantum fluids: I. Properties of the Luttinger model and their extension to the general 1D interacting spinless Fermi gas. *J. Phys. C: Solid State Phys.*, 14:2585, 1981.

[3] H. E. Bishop and J. C. Rivière. Segregation of gold to the silicon (111) surface observed by Auger emission spectroscopy and by LEED. *J. Phys. D: Appl. Phys*, 2:1635, 1969.

[4] I. R. Collins, J. T. Moran, P. T. Andrews, R. Cosso, J. D. O'Mahony, J. F. McGilp, and G. Magaritondo. Angle-resolved photoemission from an unusual quasi-one-dimensional metallic system: a single domain Au-induced 5 $\times$ 2 reconstruction of Si(111). *Surf. Sci.*, 325:45, 1995.

[5] R. Losio, K. N. Altmann, and F. J. Himpsel. Continous Transition from Two- to One-Dimensional States in Si(111)-(5 $\times$ 2)-Au. *Phys. Rev. Lett.*, 85:808, 2000.

[6] Paul C. Snijders and Hanno H. Weitering. ***Colloquium***: Electronic instabilities in self-assembled atom wires. *Rev. Mod. Phys.*, 82:307, 2010.

[7] J. N. Crain, A. Kirakosian, K. N. Altmann, C. Bromberger, S. C. Erwin, J. L. McChesney, J.-L. Lin, and F. J. Himpsel. Fractional Band Filling in an Atomic Chain Structure. *Phys. Rev. Lett.*, 90:176805, 2003.

[8] I. K. Robinson, P. A. Bennett, and F. J. Himpsel. Structure of Quantum Wires in Au/Si(557). *Phys. Rev. Lett.*, 88:096104, 2002.

[9] S. Appelfeller, S. Kuls, and M. Dähne. Tb silicide nanowire growth on planar and vicinal Si(001) surfaces. *Surf. Sci.*, 641:180, 2015.

[10] B.Z. Liu and J. Nogami. A scanning tunneling microscopy study of dysprosium silicide nanowire growth on Si(001). *J. Appl. Phys.*, 93:593, 2003.

[11] Y. Cui, J. Chung, and J. Nogami. Controlling the width of self-assembled dysprosium silicide nanowires on the Si(001) surface. *J. Phys.: Condens. Matter*, 24:045003, 2012.

[12] R. Park and H. H. Madden. Annealing changes on the (100) surface of palladium and their effect on CO adsorption. *Surf. Sci.*, 11:188, 1968.

[13] E. A. Wood. Vocabulary of surface crystallography. *J. Appl. Phys.*, 35:1306, 1964.

[14] K. Oura, V. G. Lifshits, A. Saranin, A. V. Zotov, and M. Katayama. *Suface Science (An Introduction)*. Springer, 2003.

[15] M. A. Van Hove, W. H. Weinberg, and C. M. Chan. *Low-Energy Electron Diffraction*, volume 6. Springer, 1986.

[16] E. Prince, editor. *International tables for X-ray crystallography*, volume C: Mathematical, physical and chemical tables. Wiley, 3rd edition, 2004.

[17] F. Bertram. *The structure of ultrathin iron oxide films studied by x-ray diffraction.* PhD thesis, University of Osnabrück, 2012.

[18] M. Horn von Hoegen. Growth of semiconductor layers studied by spot profile analysing low energy electron diffraction. *Z. Kristallogr.*, 214:591, 1999.

[19] M. P. Seah and W. A. Dench. Quantitative electron spectroscopy of surfaces: A standard data base for electron inelastic mean free paths in solids. *Surf. Interface Anal.*, 1:2, 1979.

[20] F. Klasing. *Indium on Silicon(111)/Low-energy electron diffraction experiments and simulations on the striped (8 × 2) surface reconstruction and on the (4 × 1) → (8 × 2) phase-transition.* PhD thesis, University of Duisburg-Essen, 2014.

[21] M. Henzler. Springer Series in Surface Sciences Vol. 3. In F. Nizzoli, K. H. Rieder, and R.F. Willis, editors, *Dynamical Phenomena at Surfaces, Interfaces and Superlattices*, pages 20–24, Berlin, Germany, 1985. Springer.

[22] J. B. Pendry. Reliability factors for LEED calculations. *J. Phys. C.: Solid State Phys.*, 13:937, 1980.

[23] I. Robinson. *Handbook on Synchrotron Radiation*, volume 3. Elsevier, 1990.

[24] P. N. Keating. Effect of invariance requirements on the elastic strain energy of crystals with application to the diamond structure. *Phys. Rev.*, 145:637, 1966.

[25] J. S. Pedersen. Surface relaxation by the keating model: A comparison with ab-initio calculations and x-ray diffraction experiments. *Surf. Sci.*, 210:238, 1989.

[26] T. Tabata, T. Aruga, and Y. Murata. Order-Disorder transition on Si(001): c(4 × 2) to (2 × 1). *Surf. Sci.*, 179:L63, 1987.

[27] K. Takayanagi, Y. Tanishiro, M. Takahashi, and S. Takahashi. Structural analysis of Si(111)-7 × 7 by UHV-transmission electron diffraction and microscopy. *Journal of Vacuum Science & Technology*, 3:1502, 1985.

[28] S. Sanna, C. Dues, W. G. Schmidt, F. Timmer, J. Wollschläger, M. Franz, S. Appelfeller, and M. Dähne. Rare-earth silicide thin films on the Si(111) surface. *Phys. Rev. B*, 93:195407, 2016.

[29] M. Franz, J. Große, R. Kohlhaas, and M. Dähne. Terbium induced nanostructures on Si(111). *Surf. Sci.*, 637-638:149, 2015.

[30] T. P. Roge, F. Palmino, C. Savall, J. C. Labrune, and C. Pirri. Er-induced $2\sqrt{3} \times 2\sqrt{3}$R30° reconstruction on Si(111): influence on the very low Er coverage silicide growth. *Surf. Sci.*, 383:350, 1997.

[31] C. Battaglia, H. Cercellier, C. Monney, M. Garnier, and P. Aebi. Stabilization of silicon honeycomb chains by trivalent adsorbates. *Europhys. Lett.*, 77:36003, 2007.

[32] A. Kirakosian, J. McChesney, R. Bennewitz, J. Crain, J. L. Lin, and F. Himpsel. One-dimensional Gd-induced chain structures on Si(1 1 1) surfaces. *Surf. Sci.*, 498:L109, 2002.

[33] E. Perkins, I. Scott, and S. Tear. Growth and electronic structure of holmium silicides by STM and STS. *Surf. Sci.*, 578:80, 2005.

[34] I. Engelhardt, C. Preinesberger, S. K. Becker, H. Eisele, and M. Dähne. Atomic structure of thin dysprosium-silicide layers on Si(1 1 1). *Surf. Sci.*, 600:755, 2006.

[35] J. E. Baglin, F. M. d'Heurle, and C. S. Petersson. The formation of silicides from thin films of some rare-earth metals. *Appl. Phys. Lett.*, 36:594, 1980.

[36] J. A. Knapp and S. T. Picraux. Epitaxial growth of rare-earth silicides on (111) Si. *Appl. Phys. Lett.*, 48:466, 1986.

[37] B. Z. Liu and J. Nogami. An STM study of the Si(001)(2 $\times$ 4)-Dy surface. *Surf. Sci.*, 488:399, 2001.

[38] C. Preinesberger, S. K. Becker, and M. Dähne. An STM study of the 2 $\times$ 7 Dysprosium-Silicide Nanowire Superstructure on Si(001). *AIP Conf. Proc.*, 696:837, 2003.

[39] B. Z. Liu and J. Nogami. An STM study of the Si(001)(2 $\times$ 7)-Gd, Dy surface. *Surf. Sci.*, 540:136, 2003.

[40] J. Bahlmann. SPA-LEED-Untersuchungen an quasi-eindimensionalen Dysprosiumsilizid-strukturen auf Si(001). bachelor thesis, University of Osnabrück, 2015.

[41] C. Preinesberger, S. K. Becker, S. Vandré, T. Kalka, and M. Dähne. Structure of $DySi_2$ nanowires on Si(001). *J. Appl. Phys.*, 91:1695, 2002.

[42] J. Nogami, A. A. Baski, and C.F. Quate. $\sqrt{3} \times \sqrt{3} \longrightarrow 6 \times 6$ Phase Transition on the Au/Si(111) Surface. *Phys. Rev. Lett.*, 65:1611, 1990.

[43] J. Kautz, M. W. Copel, M. S. Gordon, R. M. Tromp, and S. J. van der Molen. Titration of submonolayer Au growth on Si(111). *Phys. Rev. B.*, 89:035416, 2014.

[44] S. Gevers. SPA-LEED-Untersuchungen von Praseodymoxidschichten auf Si(111)-Substraten. diploma thesis, University of Osnabrück, 2007.

[45] C. Otte. Rastertunnelmikroskopie an epitaktischen Eisenschichten auf MgO(001). diploma thesis, University of Osnabrück, 2010.

[46] D. Bruns. *Structure and morphology of ultrathin iron and iron oxide films on Ag(001).* PhD thesis, University of Osnabrück, 2012.

[47] S. Ferrer and F. Comin. Surface diffraction beamline at ESRF. *Rev. Sci. Instrum*, 66:1674, 1995.

[48] J. R. Rubio-Zuazo and G. R. Castro. Hard X-ray photoelectron spectroscopy (HAXPES) ($\leq$ 15 kev) at SpLine, the Spanish CRG beamline at the ESRF. *Nucl. Instr. Meth. Phys. Res. A*, 547:64, 2005.

[49] G. R. Castro. Optical design of the general-purpose Spanish X-ray beamline for absorption and diffraction. *J. Synchrotron Rad.*, 5:657, 1998.

[50] J. Als-Nielsen and D. McMorrow. *Elements of Modern X-Ray Physics*. Wiley, 2nd edition, 2011.

[51] C. M. Schlepütz, S. O. Mariager, S. A. Pauli, R. Feidenhans'l, and P. R. Willmott. Angle caculations for (2+3)-type diffractometer: focus on area detectors. *J. Appl. Crystallogr.*, 44:73, 2010.

[52] C. Ponchut, J. M. Rigal, J. Clément, E. Papillon, A. Homs, and S. Petitdemange. MAXIPIX, a fast readout photon-counting X-ray area detector for synchrotron applications. *J. Instrum.*, 6:C01069, 2011.

[53] C. M. Schlepütz, R. Herger, P. R. Willmott, B. D. Patterson, O. Bunk, Ch. Brönnimann, B. Henrich, G. Hülsen, and E. F. Eikenberry. Improved data acquisition in grazin-incidence X-ray scattering experiments using a pixel detector. *Acta Crystallogr. Sect. A*, 61:418, 2005.

[54] S. C. Erwin. Self-Doping of Gold Chains on Silicon: A New Structural Model for Si(111)-(5 $\times$ 2)-Au. *Phys. Rev. Lett.*, 91:206101, 2003.

[55] I. Barke, F. Zheng, S. Bockenhauer, K. Sell, V. v. Oeynhausen, K. H. Meiwes-Broer, S. C. Erwin, and F. J. Himpsel. Coverage-dependent faceting of Au chains on Si(557). *Phys. Rev. B*, 79:155301, 2009.

[56] S. C. Erwin, I. Barke, and F. J. Himpsel. Structure and energetics of Si(111)-(5 $\times$ 2)-Au. *Phys. Rev. B*, 80:155409, 2009.

[57] T. Abukawa and Y. Nishigaya. Structure of the Si(111)-(5 $\times$ 2)-Au Surface. *Phys. Rev. Lett.*, 110:036102, 2013.

[58] S. G. Kwon and M. H. Kang. Identification of the Au Coverage and Structure of the Au/Si(111)-(5 $\times$ 2) Surface. *Phys. Rev. Lett.*, 113:086101, 2014.

[59] T. Shirasawa, W. Voegeli, T. Nojima, Y. Iwasawa, Y. Yamaguchi, and T. Takahashi. Identification of the Structure Model of the Si(111)-(5 $\times$ 2)-Au Surface. *Phys. Rev. Lett.*, 113:165501, 2014.

[60] C. Hogan, E. Ferraro, N. McAlinden, and J. F. McGilp. Optical fingerprints of Si honeycomb chains and atomic gold wires on the Si(111)-(5 $\times$ 2)-Au surface. *Phys. Rev. Lett.*, 111:087401, 2013.

[61] K. Seino and F. Bechstedt. First-prinicples calculations of energetics and electronic structure for reconstructed Si(111)-(5 × n)-Au surfaces. *Phys. Rev. B*, 90:165407, 2014.

[62] J. D. O'Mahony, C. H. Patterson, J. F. McGilp, F. M. Leibsle, P. Weightman, and C. F. J. Flipse. The Au-induced 5 × 2 reconstruction on Si(111). *Surf. Sci.*, 277:L57, 1992.

[63] A. Kirakosian, J. Crain, J.-L. Lin, J. McChesney, D. Petrovykh, F. Himpsel, and R. Bennewitz. Silicon adatoms on the Si(1 1 1) 5 × 2-Au surface. *Surf. Sci.*, 532-535:928, 2003.

[64] J. S. Kasper and K. Lonsdale, editors. *International tables for X-ray crystallography*, volume 2 (Mathematical Tables). Kynoch Press, 1972.

[65] O. Bunk. *Bestimmung der Struktur komplexer Halbleiter-Oberflächenrekonstruktionen mit Röntgenbeugung*. PhD thesis, University of Hamburg, 1999.

List of Figures

List of Tables

Danksagung

Als allererstes möchte ich mich bei Prof. Dr. Joachim Wollschläger für die Betreuung meiner Doktorarbeit, für die Unterstützung bei etlichen Synchrotron-Messzeiten und für die zahlosen Diskussionen über die Experimente und die aus ihnen gewonnen Messdaten bedanken.
Außerdem möchte ich mich bei der Deutschen Forschungsgemeinschaft (DFG) für die Finanzierung meiner Promotionsstelle im Rahmen der Forschergruppe FOR1700 bedanken. Des Weiteren bedanke ich mich bei allen Studierenden die ich während ihrer Abschlussarbeit betreuen durfte für die gute Zusammenarbeit. Hier sind insbesondere Jascha Bahlmann und Robert Oelke hervorzuheben, deren Messergebnisse Eingang in zwei meiner Veröffentlichungen gefunden haben. Des Weiteren möchte ich mich bei Prof. Dr. Simone Sanna, Prof. Dr. Mario Dähne, Prof. Dr. Wolf Gero Schmidt, Christof Dues, Stephan Appelfeller und Dr. Martin Franz für die Zusammenarbeit im Rahmen unserer Forschergruppe und unserer gemeinsamen Veröffentlichungen bedanken.
Ausserdem möchte ich mich bei all den Leuten bedanken die mich bei den diversen Synchroton-Messzeiten unterstützt haben. Besonderer Dank gilt hierbei Dr. Henrik Wilkens, Dr. Tobias Schemme, Waldemar Schreiber und Jari Rodewald, welche immer mit vollem Einsatz bei der Sache waren, selbst wenn die Experimente einmal nicht wie erhofft verliefen. Des Weiteren möchte ich mich bei unserem technischen Assisten Gregor Steinhoff für die tatkräftige Unterstützung bei der Vorbereitung von Experimenten in unseren Heimlaboren und bei den Mitarbeitern der Feinmechanischen Werkstatt und der Werkstatt für Elektronik für die Hilfe bei der Reparatur und Konstruktion von Laborgeräten/UHV-Komponenten bedanken.
Ein großes Dankeschön geht an die komplette aktuelle und ehemalige Arbeitsgruppe Wollschläger, für eine wunderbare Arbeitsatmosphäre in der es immer Spaß gemacht hat zu arbeiten.
Last but not least, möchte ich mich insbesondere bei meiner Mutter, meinem Stiefvater und bei meinem Vater für die jahrelange Unterstützung in allen Bereichen meines Lebens bedanken. Ihr seid die besten Eltern die man sich wünschen kann und ohne euch wäre das Ganze in dieser Form nicht möglich gewesen. Vielen, vielen Dank!

Erklärung

Hiermit erkläre ich an Eides Statt, die vorliegende Abhandlung selbstständig und ohne unerlaubte Hilfe verfasst, die benutzten Hilfsmittel vollständig angegeben und noch keinen Promotionsversuch unternommen zu haben.

Osnabrück, 27.09.2017
Frederic Yaw Timmer